

On the self-regulation of intense star-formation in galaxies at $z=1-3^*$

M. D. Lehnert^{1,2}, L. Le Tiran¹, N. P. H. Nesvadba³, W. van Driel¹, F. Boulanger³, and P. Di Matteo¹

¹ GEPI, Observatoire de Paris, UMR 8111, CNRS, Université Paris Diderot, 5 place Jules Janssen, 92190 Meudon, France

² Institut d'Astrophysique de Paris, UMR 7095, CNRS, Université Pierre et Marie Curie, 98 bis Bd Arago, 75014 Paris, France

³ Institut d'Astrophysique Spatiale, UMR 8617, CNRS, Université Paris-Sud, Bâtiment 121, 91405 Orsay Cedex, France

Accepted, Received

ABSTRACT

We have analyzed the properties of the H α and [NII] λ 6583 rest-frame optical emission lines of a sample of 53 intensely star forming galaxies at $z=1.3$ to 2.7 observed with SINFONI on the ESO-VLT. Similar to previous authors, we find large velocity dispersions in the lines, σ =few 10-250 km s⁻¹. Our data agree well with simulations where we applied beam-smearing and assumed a scaling relation of the form: velocity dispersion is proportional to the square root of the star-formation intensity (star-formation rate per unit surface area). We conclude that the dispersions are primarily driven by star formation. To explain the high surface brightness and optical line ratios, high thermal pressures in the warm ionized medium, WIM, are required ($P/k \gtrsim 10^6-10^7$ K cm⁻³). Such thermal pressures in the WIM are similar to those observed in nearby starburst galaxies, but occur over much larger physical scales. Moreover, the relatively low ionization parameters necessary to fit the high surface brightnesses and optical line ratios suggest that the gas is not only directly associated with regions of star formation, but is wide spread throughout the general interstellar medium. Thus the optical emission line gas is a tracer of the large scale dynamics of the bulk of the ISM.

We present a simple model for the energy input from young stars in an accreting galaxy, to argue that the intense star-formation is supporting high turbulent pressure, which roughly balances the gravitational pressure and thus enables distant gas accreting disks to maintain a Toomre disk instability parameter $Q \sim 1$. For a star formation efficiency of 3%, only 5-15% of the mechanical energy from young stars that is deposited in the ISM is needed to support the level of turbulence required for maintaining this balance. Since this balance is maintained by energy injected into the ISM by the young stars themselves, this suggests that star formation in high redshift galaxies is self-regulating.

Key words. galaxies: evolution — galaxies: formation — galaxies: kinematics and dynamics — galaxies: ISM — galaxies: star formation

1. Introduction

Galaxies exhibit a wide range of phenomena, some of which appear to have been more important in the distant Universe than today. The global co-moving star-formation rate was higher by an order of magnitude (Madau et al. 1996), and so were the specific star-formation rates (Elbaz et al. 2007; Daddi et al. 2007). Morphologies were increasingly irregular, an observation that cannot be explained with extinction alone (Conselice et al. 2008). Processes like starburst-driven outflows are obvious and ubiquitous in samples of high redshift galaxies (e.g., Shapley et al. 2003; Steidel et al. 2010) compared to only a small fraction of galaxies today (Lehnert & Heckman 1996). The merger rate is also likely to be much higher (de Ravel et al. 2009). The gas infall rates of nearby galaxies are apparently low, but they were likely much higher in the early Universe (Croton et al. 2006). Today, the Universe can be considered in the “age of secular evolution”, but until about 8 Gyrs ago it was in the “age of feedback and self-regulation”. It is the mix of physical processes during their early evolution that shaped the characteristics of the ensemble of the galaxies we observe today.

Understanding this complexity and the relative contribution of the physical processes that shaped distant galaxies is required before we can consider our understanding of galaxies in any sense complete. With the higher activity levels of galaxies at $z \sim 1-5$ relative to today it is difficult to gauge the importance of each process by mere analogy. This requires careful, direct observations of distant galaxies.

Of significant concern in this pursuit is that obtaining detailed spatial information from distant galaxies is hampered by the large impact of cosmological surface brightness dimming, e.g. by a factor ~ 150 for $z=2.5$. This implies that only the highest surface brightness galaxies are spatially resolved with integral field spectroscopy or in continuum imaging. It also biases the samples where we can detect spatially extended emission line gas to galaxies which have intense star formation over many tens of kpc² or extended emission line regions excited by powerful active galactic nuclei (e.g., Nesvadba et al. 2006, 2008).

Observations of intensely star-forming galaxies at $z \sim 2$ with bright, extended line emission reveal remarkably broad line widths implying important random, and presumably (at least partially) turbulent, gas motions. Limited by the ~ 1 -few kpc resolution of current spectrographs, the observed line widths reflect the blended bulk and turbulent gas motions on kpc scales. In galaxies where velocity gradients are spatially resolved, both motions have very similar amplitudes, unlike in nearby galaxies where line widths are much smaller than cir-

* Data obtained as part of program IDs: 074.A-9011, 075.A-0318, 075.A-0466, 076.A-0464, 076.A-0527, 076.B-0259, 077.B-0079, 077.B-0511, 078.A-0055, 078.A-0600, 079.A-0341 and 079.B-0430 at the ESO-VLT.

cular velocities (Law et al. 2007, 2009; Förster Schreiber et al. 2009; Epinat et al. 2009, 2010, 2012). This requires either a more intense, or perhaps more efficient, source or an additional source of turbulent energy at high redshift. The possible sources for energizing the turbulence remain the subject of significant controversy. Some authors suggest that the turbulent cascade is primarily initiated by shear and large scale gravitational or fluid instabilities, perhaps further energized by cosmological gas accretion (Brooks et al. 2009; Kereš et al. 2009; Dekel et al. 2009a; Elmegreen & Burkert 2010), while others give a significant role to the energy injection from young stars (e.g., Elmegreen & Scalo 2004; Cox 2005; Ferrara 1993; Norman & Ferrara 1996). However, the dichotomy between gravitational and stellar sources of energy is largely artificial as both no doubt play important roles. Supersonic turbulence can provide global support to the ISM, but it naturally produces density enhancements that may collapse locally and may subsequently form stars or dissolve. Global star formation in galaxies appears to be controlled by the balance between gravity and turbulence (Mac Low & Klessen 2004). This balance is moderated by the importance of each form of energy injection, which on the largest scales depends on the rate and scale at which it is injected, and on how rapidly the energy cascades and dissipates in various phases, and over what time and size scales (e.g., Elmegreen & Scalo 2004). None of these variables are well constrained in distant galaxies. To some extent, the global regulation of star formation mirrors that taking place on the smallest scales, where the dissipation of turbulent energy in self-gravitating clouds is important for regulating star formation within these clouds.

Lehnert et al. (2009) found that the velocity dispersions, σ , of optical emission-line gas in intensely star-forming galaxies at $z \sim 2$ scale with the star-formation rate per unit area (star-formation intensity, Σ_{SFR}) as $\sigma \propto \Sigma_{\text{SFR}}^{0.5}$ (see also Swinbank et al. 2012; Menéndez-Delmestre et al. 2013). They suggested that at a very simple level, such a relationship would be expected if the lines were broadened by the mechanical energy injection from young stars (Dib et al. 2006). Subsequently, Green et al. (2010) came to similar conclusions from observing strongly star-forming galaxies at low redshifts which had similar overall $\text{H}\alpha$ luminosities as galaxies observed at $z \sim 2$ with integral field spectroscopy (Lehnert et al. 2009). More recently, and through an analytical approach, Ostriker & Shetty (2011) found that such a relationship might be the natural outcome of dense ($\Sigma_{\text{gas}} \sim \text{few } 100 \text{ M}_{\odot} \text{ pc}^{-2}$), star-forming gas disks which are regulated through the momentum input from star formation. Compared to the other possible sources such as gas accretion, star-formation intensity in high- z galaxies can be constrained observationally, e.g. by measuring $\text{H}\alpha$ luminosities and spatial distributions, although heavily extinguished regions may have their intensities underestimated.

A number of authors subsequently pointed out that this relationship is also consistent with the Toomre disk stability criterion (e.g., Krumholz & Dekel 2010). Although not discussed in their work, a Toomre parameter $Q \sim 1$ characteristic of gas disks which are marginally unstable against star formation leads to a relationship of the type observed, $\sigma \propto \Sigma_{\text{SFR}}^{0.6-0.7}$, if these galaxies follow the Schmidt-Kennicutt relation. Burkert et al. (2010) develop this idea further by arguing that disks must stay close to the gravitational stability line. They suggest that large scale gravitational instabilities will generate density and velocity irregularities which drive turbulence and heat the gaseous disk. This process saturates close to the instability line and thus, Burkert et al. (2010) argue that gravitational forcing is sufficient to explain the

highly turbulent gas. Elmegreen & Burkert (2010) find that their analytical model of intensely star-forming, fragmenting disks can reproduce the observed velocity dispersions in high redshift galaxies if Q is set equal to 1, suggesting that whatever the mechanism responsible for driving galaxies towards the line of instability, it can reproduce the observations.

The basic difficulty is that observing velocity gradients and line widths consistent with marginally Toomre-stable disks only implies that distant star-forming galaxies are in a state where they can form stars intensely, but it does not purport to explain the source of the turbulence. Galaxies at $z \sim 2$ appear to maintain their high gas turbulence over long star-formation time scales of several 10^8 yrs, and maintaining $Q \sim 1$ over similar timescales is only possible if turbulent dissipation is balanced by the injection of turbulent energy over similar length of time. Since turbulent energy dissipates rapidly, on only a dynamical time (Mac Low 1999), this seems difficult to ensure with gravity alone over the extended star-formation periods (Elmegreen & Burkert 2010). Moreover, gravitationally-driven processes alone are perhaps insufficient for producing even the relatively modest dispersion observed in the warm neutral and ionized medium of nearby galaxies (Tamburro et al. 2009; Leroy et al. 2008). Correlations between star-formation rate and $\text{H}\alpha$ velocity dispersions in nearby galaxies (Tamburro et al. 2009) as well as the decrease in CO line dispersions with radius in some nearby galaxies (Wilson et al. 2011) favor an important, but perhaps not dominant, contribution from the energy injection by supernovae and stellar winds in regulating the turbulence of the ISM in nearby galaxies. The same also appears true for intensely star-forming relatively nearby galaxies with properties similar to high redshift Lyman break galaxies (Basu-Zych et al. 2009; Gonçalves et al. 2010).

Here we present new observational data on how star formation intensities and gas kinematics in high-redshift galaxies are related, extending our initial sample from 11 galaxies to 53, and covering a larger redshift range. Apart from putting our previous claims on statistically more robust grounds this also allows us to demonstrate the effects of surface-brightness dimming directly. We discuss the inevitable biases in all studies of star formation in high-redshift galaxies related to surface-brightness dimming and beam-smearing from our data, and demonstrate that our results are not dominated by these effects. With this larger sample we confirm the results of Lehnert et al. (2009) that the ISM in the observed high-redshift galaxies has very high pressures compared to galaxies at low redshift. We argue that this enables star formation in these galaxies to be self-regulated, and demonstrate that self-regulation leads very naturally to a Toomre parameter, $Q \sim 1$, generalizing the analytical model first presented by Elmegreen & Burkert (2010). We further paint a picture of what the optical emission line gas may be showing us about the turbulent cascade and its impact on star formation in high redshift galaxies.

Throughout the paper we adopt a flat $H_0 = 70 \text{ km s}^{-1} \text{ Mpc}^{-3}$ cosmology with $\Omega_{\Lambda} = 0.7$ and $\Omega_M = 0.3$.

2. Source characteristics

Our sample of 53 galaxies was observed with SINFONI on the ESO-VLT. Their basic properties of the 53 galaxies are presented in Table 1. They span a redshift range of $z = 1.3-2.7$ (Fig 1). For details of the observations of the galaxies in this sample see the summaries in e.g. Lehnert et al. (2009); Förster Schreiber et al. (2006, 2009). All were reduced by us in a similar way as previously described by Lehnert et al. (2009).

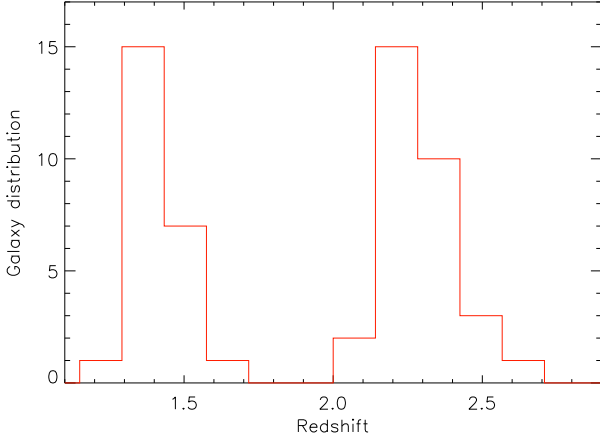


Fig. 1. Redshift distribution of our sample of galaxies. The two observed redshift ranges of the $H\alpha$ and $[NII] \lambda 6583$ lines ($z < 1.8$ and $z > 2$) are due to atmospheric transmission and the limited wavelength coverage of the H- and K-bands.

The data, which were retrieved from the ESO archives, were taken for a variety of programs and the selection of the galaxies is rather inhomogeneous. As we are not performing a population study, for the purposes of this paper, this is adequate. The key to our sample is that all galaxies have sufficiently high $H\alpha$ surface brightness to obtain spatially resolved line maps in a few hours integration time (which is typical for SINFONI observations of distant galaxies). Because of this, our results are only applicable to galaxies with high star-formation intensity (star-formation rate per unit area) which necessitates a process that is able to drive intense star-formation for 100 Myrs or more (Erb et al. 2006) and my introduce a bias. However, it should be pointed out that the characteristics of the ensemble of galaxies studied here are similar to those of the general distant star-forming galaxy population. Specifically, the galaxies in our sample for which the specific star formation rate has been estimated (a majority; see Förster Schreiber et al. 2009, 2011; Genzel et al. 2011; Vergani et al. 2012, and references therein), lie along or near the “main sequence of star formation” for redshifts between 1 and 2 (e.g. Elbaz et al. 2007; Daddi et al. 2007; Elbaz et al. 2011).

The observations reach surface brightness detection limits in $H\alpha$ of $\sim 2 \times 10^{-19}$ erg s $^{-1}$ cm $^{-2}$ pixel $^{-1}$ (for the 125 mas pixel $^{-1}$ scale and averaged over 3×3 pixels; “mas” is milliarcseconds). The spectral resolution is FWHM ~ 115 and ~ 150 km s $^{-1}$ in the K and H bands, respectively. The observed surface brightnesses range from about $3.6\text{--}34 \times 10^{-18}$ erg cm $^{-2}$ s $^{-1}$ arcsec $^{-2}$ and the objects have isophotal radii, at their surface brightness detection limits, of 1-2 arcsec 2 , or on average $\sim 7 \pm 2$ kpc (corresponding to an isophotal area of $\sim 150 \pm 40$ kpc 2). The point-spread function FWHM of the data is $\sim 0''.6$, which at $z=2$ represents an area of ~ 20 kpc 2 , so we have generally ~ 8 spatial resolution elements per object. With such low spatial resolution, it is necessary to discuss the impact of beam smearing on the characteristics of our data (discussed in detail in § 4). In the present analysis, we will formally define the isophotal radius, r_{iso} , as $r_{\text{iso}} = (A_{\text{iso}}/\pi)^{1/2}$, where A_{iso} is the isophotal area, i.e. the total area of all pixels above the $3\text{-}\sigma$ surface brightness limit of the data (Table 1).

The total $H\alpha$ luminosities of all galaxies in our sample are above 10^{41} erg s $^{-1}$ and most are above $\sim 10^{42}$ erg s $^{-1}$. $H\alpha$ luminosities in this range imply an average star-formation rate of $\sim 70 M_{\odot}$ yr $^{-1}$. However, as these are not corrected for extinction our

estimates are lower limits. For a sub-sample of these galaxies we have $H\beta$ estimates, and the line ratios of $H\alpha$ to $H\beta$ suggest relatively modest extinction corrections to the star-formation rates, of a factor of few (Lehnert et al. 2009).

3. Surface brightness limits and selection effects

Due to cosmological surface brightness dimming, over the redshift range of a factor ~ 2 in our sample there is about a factor of 5 difference in the faintest rest-frame line emission surface brightness levels that can be probed, whereas the physical dimensions in the rest frame, i.e., length per arcsec, changes by only about 5%. Given this strong impact of cosmological surface brightness dimming, it is worth repeating the conclusion from Lehnert et al. (2009) that even the lowest redshift sources in our SINFONI sample are extreme compared to galaxies in the local volume, where only the most intense starbursts have such high $H\alpha$ surface brightness, and this on considerably smaller physical scales only.

The total range in surface brightness probed by the SINFONI observations of our ensemble of galaxies is ≈ 20 (Fig. 2). For purposes of this comparison and others, we constructed 2-dimensional histograms which show the frequency of occurrence of various pairs of values in all pixels of our data sets, after smearing to the spatial and spectral resolution of the real SINFONI observations – for example, surface brightness versus projected distance or $H\alpha$ line width versus star-formation rate intensity. Using the frequency of occurrence is a clearer way of visualizing various relationships than showing all single pixels and emphasizes the continuity of the data.

To investigate the dependence of the range of surface brightnesses probed by our data and its influence on the observed galaxy isophotal size, we divided our galaxies into 4 bins of equal galaxy number based on their isophotal areas (Fig. 3). For the 3 bins with the largest average isophotal sizes (≥ 1.4 arcsec 2), the observed dynamic range in surface brightness goes up to ~ 20 and is typically about 15. However, for the apparently smaller galaxies, the dynamic range of the observations is only about a factor of 3. The relationship between surface brightnesses and projected distance is the same for all bins, indicating that their individual declines in surface brightness follow the same trend. The observations imply two things. First, although the effects of beam smearing cannot be ignored, as we will discuss extensively in the next sections, it does not dominate the overall distribution of the surface brightness (i.e., the distribution does not simply represent the point-spread-function, PSF, of the observations). Second, it implies that the reason the apparently small galaxies appear small is that the surface brightness detection limits of the observations are too high to detect their extended emission. As noted above, this is not simply due to the physical scale of the galaxies changing across our redshift range, as this effect amounts to only $\sim 5\%$. While we do not show it here, there is a crude trend for the galaxies with the highest total $H\alpha$ fluxes to also have the largest isophotal sizes. Again, this suggests that we are limited by the overall dynamic range of the data and by the impact of surface brightness dimming, but not by differences in the intrinsic isophotal sizes of the galaxies (Fig. 4). This is an important point to bear in mind when reading this paper.

Furthermore, if the trends in surface brightness and total $H\alpha$ luminosity were dominated by cosmological surface brightness dimming, which is proportional to $(1+z)^4$, we would expect our data to show a slope of about 4 in a plot of the logarithmic relation between $H\alpha$ luminosity and isophotal area and indeed, we find such a trend (Fig. 4). The range in surface brightness detec-

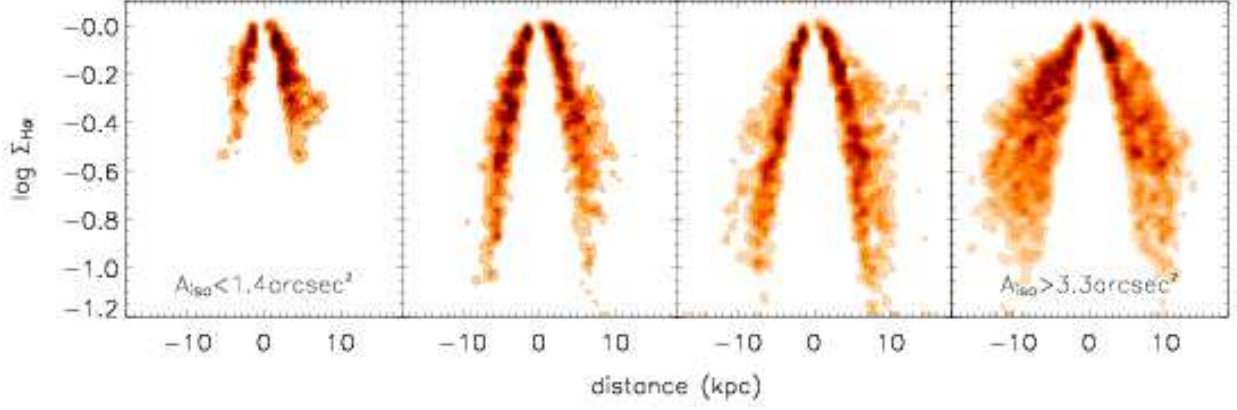


Fig. 3. Two-dimensional histograms of the relative frequency of occurrence of normalized $H\alpha$ surface brightness values versus the projected distance for galaxies in 4 equal-size bins in galaxy number selected on their isophotal area (A_{iso}). The relative frequency of occurrence is scaled in the same way as in Fig. 2. From left to right, each panel represents an increasing angular size (i.e., $A_{\text{iso}} < 1.4 \text{ arcsec}^2$, $1.4 \text{ arcsec}^2 \geq A_{\text{iso}} < 2.5 \text{ arcsec}^2$, $2.5 \text{ arcsec}^2 \geq A_{\text{iso}} < 3.3 \text{ arcsec}^2$ and $A_{\text{iso}} \geq 3.3 \text{ arcsec}^2$). The values of r_{iso} , which is derived from A_{iso} , for individual galaxies are given in Table 1. The galaxies with the smaller dynamic range (higher surface brightness detection limits) in the data are also smaller in isophotal size.

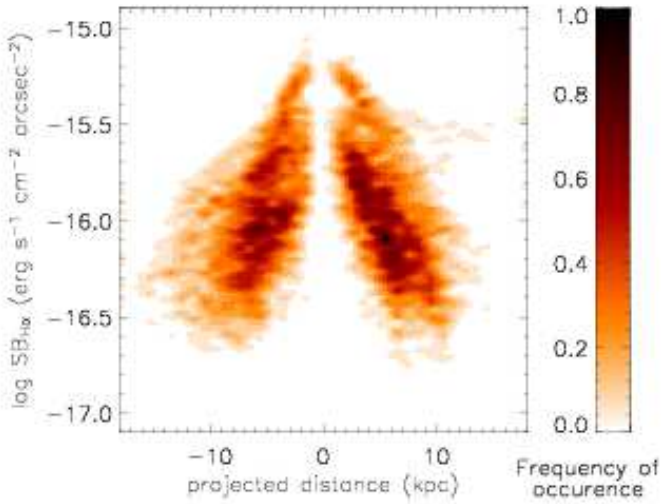


Fig. 2. A 2-dimensional histogram of the frequency of occurrence of pixel values of $H\alpha$ surface brightness versus projected physical distance for the entire sample. As shown in the color bar, the darkest regions have the highest frequency of occurrence. The surface brightness has not been corrected for cosmological dimming. The zero of the projected distance was chosen to be the symmetry point in either the $H\alpha$ velocity field or of $3\text{-}\sigma$ isophotes in the $H\alpha$ surface brightness map.

tion limits in our data trace out the ranges in size and luminosity we observe in our sample of galaxies. In addition, this confirms that at the high redshift end of our sample the intrinsic surface brightnesses are very high and that they generally decline with redshift.

4. The effect of beam smearing

In Lehnert et al. (2009), we proposed that the $H\alpha$ emission line velocity dispersions of the high surface brightness spatially-

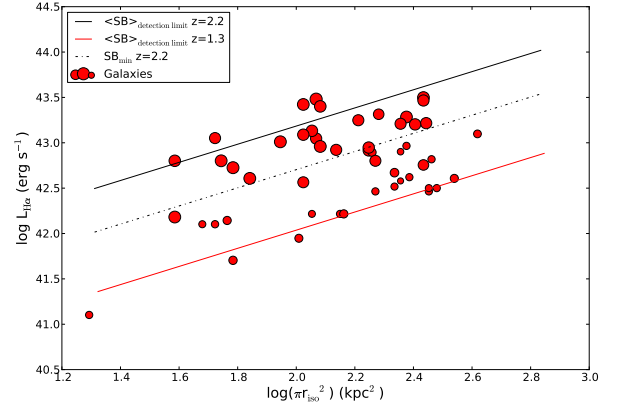


Fig. 4. Plot of $H\alpha$ luminosities versus isophotal area for the galaxies in our sample (red circles). The size of each circle is proportional to the redshift of the galaxy, with larger circles denoting higher redshifts (range in z is 1.3–2.7). The two solid lines show the relationship between luminosity and area for the average surface brightness detection level of galaxies, $1.1 \times 10^{-17} \text{ erg s}^{-1} \text{ cm}^{-2} \text{ arcsec}^{-2}$ (black for galaxies at $z=2.2$ and red for $z=1.3$, respectively). The dot-dashed line shows the relationship for the minimum surface brightness detection limit of $3.6 \times 10^{-18} \text{ erg s}^{-1} \text{ cm}^{-2} \text{ arcsec}^{-2}$ for all galaxies with $z \approx 2.2$. See Table 1 for the $H\alpha$ luminosities, isophotal radii and surface brightness detection limits.

resolved galaxies observed with SINFONI (and other near-infrared integral field units) could be explained by the mechanical output of young stellar populations within those galaxies. In fact, we framed the argument in the context of an overly simplified energy injection model of the form, $\sigma = (\epsilon \Sigma_{\text{SFR}})^{1/2}$, where σ is the $H\alpha$ velocity dispersion, ϵ is the coupling efficiency of the mechanical energy output to the interstellar medium and Σ_{SFR} is the star-formation intensity. The energy due to the young stars is given by population synthesis models (Leitherer et al. 1999). Using scaling relations based on models and observations of

nearby galaxies, we were able to explain the trends between dispersion and star-formation intensity with no free parameters (see Lehnert et al. 2009, for details of the scalings used in this analysis).

However, the limited spatial resolution of integral field spectroscopy of $z \sim 2$ galaxies causes an artificial broadening of the emission lines due to large-scale kinematics, which can result in a significant radial velocity gradient across each pixel. While we argued that this would not have an important impact on our results in Lehnert et al. (2009) based on some simple modeling, we now feel it is important to revisit this issue in a more complete and detailed way.

4.1. Construction of artificial IFU observations

In order to study the effect of beam smearing, we used the simulation of an isolated galaxy already presented in Di Matteo et al. (2008) which was made using a Tree-SPH code (see Semelin & Combes 2002; Di Matteo et al. 2009; Chilingarian et al. 2010, for a description). This model has a high gas mass fraction (50%) and the galaxy was evolved in isolation, without companions or tidal interactions (Qu et al. 2011). We allowed the disk to go unstable against star-formation and it developed a “clumpy” morphology which evolved with time (see Di Matteo et al. 2008, for details of the initial conditions and evolution of the simulation). Intrinsically, our simulations show low gas velocity dispersions, of-order 10 km s^{-1} (or less), which are roughly constant with radius and a rotation speed of $\sim 220 \text{ km s}^{-1}$ which implies a $v/\sigma \approx 20$. From this simulation, we produced maps of the star-formation intensity, radial velocity field and velocity dispersion (Fig. 5). For our primary analysis, the simulation was viewed at an inclination angle of 45° and scaled to have a projected rotational amplitude of 110 km s^{-1} , a value derived from the average intrinsic full width at half maximum of the integrated spectra of our sample. This implies a rotation speed of about 160 km s^{-1} .

We then degraded the resolution of the simulations to produce synthetic observations similar to what we observed with SINFONI. We adopted a single redshift ($z=2$) for determining the scalings in the synthetic observations – the exact redshift chosen does not matter much as the physical scale per angular projected size (kpc arcsec^{-1}) changes little ($\sim 5\%$) over the redshift range of our sources. We also took into account the instrumental spectral resolution, the seeing using a FWHM for a Gaussian distributed PSF of $0''.6$ and added an amount of noise to the synthetic data consistent with the observations. The artificial datacubes created in this way were then analyzed using the same procedures as the real SINFONI observations.

In the following analysis, we will focus on the impact of beam smearing on the interpretation of the underlying cause of the high dispersion observed in distant galaxies with spatially-resolved line emission observations.

In Lehnert et al. 2009 we proposed that the dispersion is proportional to the star-formation intensity. For our analysis of the effects of beam smearing, we make a comparison between the analogs produced using two sets of scaling relations for the velocity dispersions: (1) the dispersions taken directly from the simulation, σ_{sim} , and (2) a function of the star formation intensity $\sigma = 140 \sqrt{\Sigma_{\text{SFR}}} \text{ km s}^{-1}$ – see Lehnert et al. (2009) for details. The resulting $\text{H}\alpha$ flux and kinematics maps made with our artificial SINFONI data sets and applying these two different types of dispersion show, as expected, that the surface brightness distribution is now smoother than in the original simula-

tion (Fig. 6). The star-formation intensities – the star-formation rate per unit area – are related to the $\text{H}\alpha$ surface brightness by a simple scaling (e.g. Kennicutt 1998). We use this scaling to produce the $\text{H}\alpha$ surface brightness distribution which is subsequently beam smeared.

4.2. Effect of beam smearing on star-formation intensities

The areas of intrinsically high star formation intensity are blended after smearing the data, which lowers their intensities (Fig. 6). Whether or not such peaks in the star-formation intensity can be observed in principle depends on their relative distribution and peak intensity relative to their surroundings within one or two PSFs (cf. Figs. 5 and 6). However, Fig. 7 demonstrates that, after smearing, the simulated final radial distribution of surface brightness is consistent with what we observe. The similarity seen does not depend on the underlying velocity dispersion distribution assumed in the construction of the synthetic data.

The star-formation intensities from the simulation decline by $\lesssim 25\%$ after beam smearing. While the precise value of this decrease is likely to depend on the initial spatial distribution of the surface brightness, it is always going to be small. The total star-formation rate, which in the simulations is typically about $60 M_\odot \text{ yr}^{-1}$, remains essentially unchanged after making an artificial SINFONI data set. The largest impact of smearing is on the distribution of the star-formation intensities and in losing the lowest surface brightness emission because of noise and the relatively low dynamic range of the data.

4.3. Effect of beam smearing on velocity dispersions

Since we have assumed two quite different relationships between velocity dispersions and star-formation intensity, it is in the resulting velocity dispersions that we see the most dramatic differences. In the model with σ_{sim} , the dispersion is low (a few to 10 km s^{-1}) and almost constant as a function of radius and star-formation intensity (Fig. 8, left panel). In the synthetic observations however, the beam smearing by the PSF ($\text{FWHM}=0''.6$) and the low spectral resolution of the data broadens all lines by about $\sim 40 \text{ km s}^{-1}$ and the noise in the data increases the scatter about this mean rise in the dispersions. Even though we correct for the intrinsic resolution of the spectrograph, at relatively low S/N we tend to over-estimate the widths of lines that are only marginally resolved. Our results suggest that for galaxies with roughly constant and low dispersions ($\sim 40 \text{ km s}^{-1}$), a spectrograph like SINFONI will tend to over-estimate the intrinsic widths of the lines but still produce a roughly constant trend of dispersion with star-formation intensity.

For the model where the simulation dispersions are scaled as $\sigma = 140 \sqrt{\Sigma_{\text{SFR}}} \text{ km s}^{-1}$, there are almost no differences between the mean velocity dispersions from the simulation itself and the artificial data sets (Fig. 8, right panel). Because of the large range of the scaled velocity dispersions, there is little effect of beam smearing on the average velocity dispersion. Looking at the pixel-by-pixel quantities, we obviously lose the relatively rare regions and peaks with the highest velocity dispersions (over 200 km s^{-1}). However, as suggested by the average and intrinsic dispersions, the decrease in the values (ranges and averages) is not large, even after the smoothing to low spatial and relatively low spectral resolution. Again, because of the loss of the lowest surface brightness regions, we also tend to lose information on the areas with the lowest velocity dispersions. However, in spite

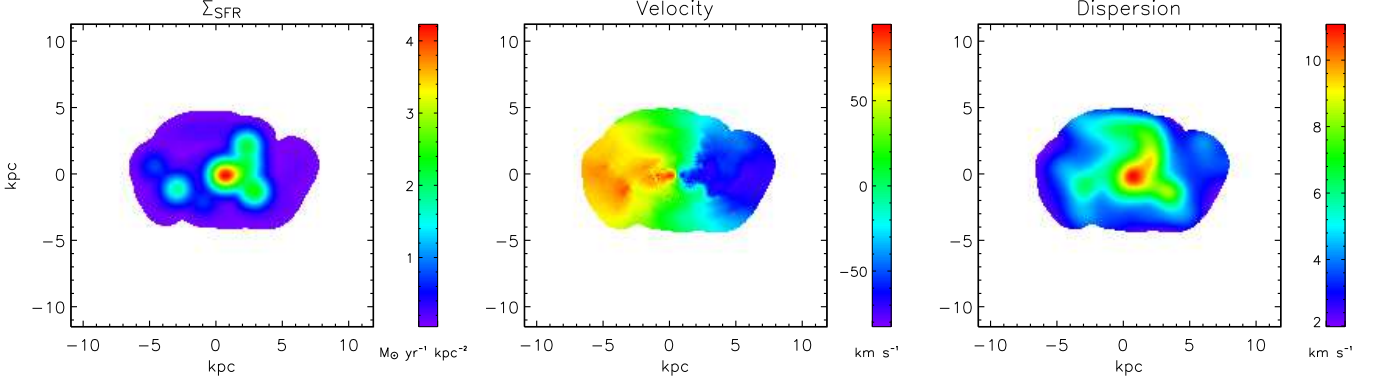


Fig. 5. Output from the simulation of a star-forming disk galaxy as it would appear at $z=2$ before it was beam smeared. Shown are the distribution of the star-formation rate intensity (left panel), $H\alpha$ velocity field (center panel) and $H\alpha$ dispersion map (right panel). The galaxy is projected at an inclination angle of 45° relative to face-on. The scale on the axes is in kpc and the kinematic axis is horizontal. Despite the different units (kpc vs. arc seconds), we note that the sizes of these panels and those in Fig. 6 are similar, for ease of direct comparison.

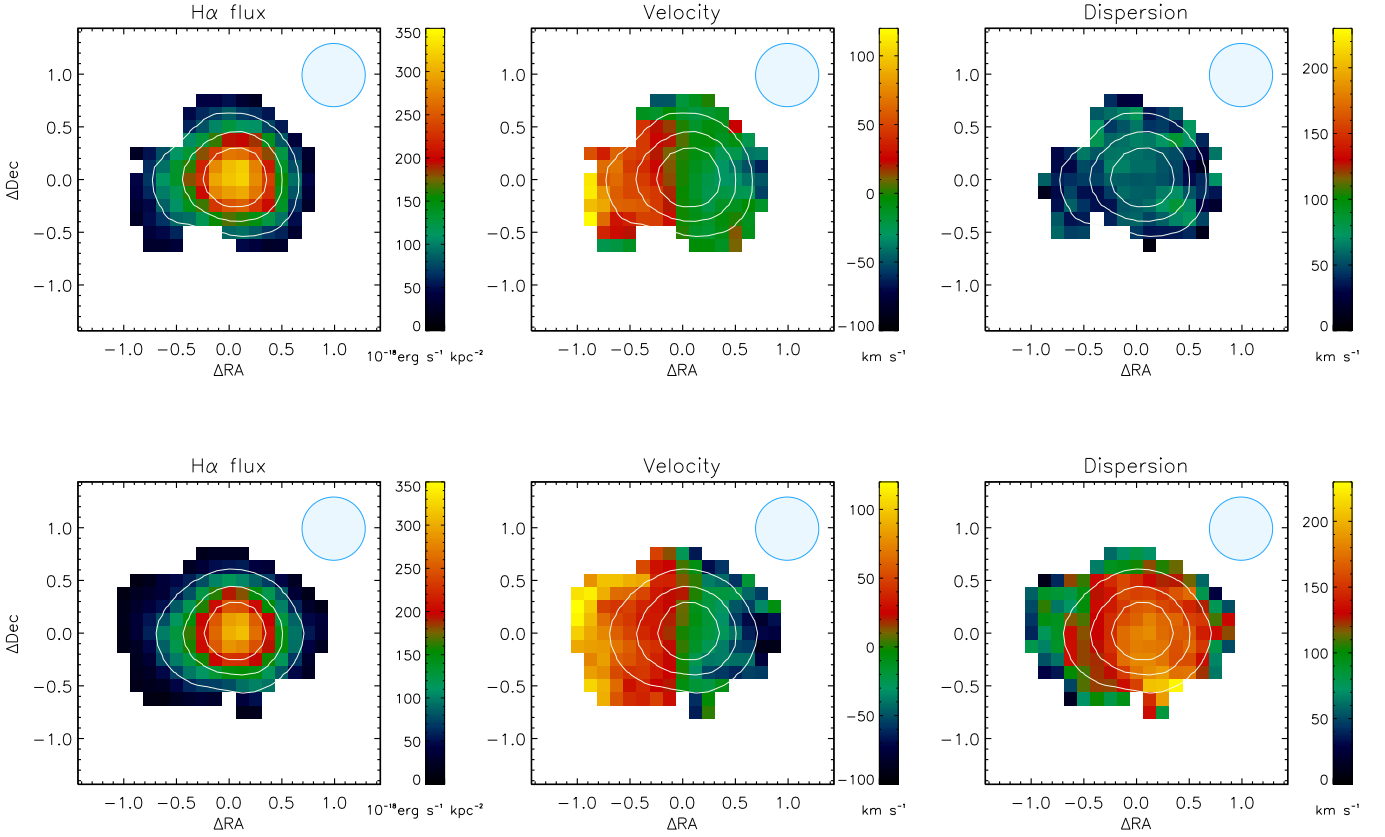


Fig. 6. Results of the simulated data sets of a star-forming disk galaxy at $z=2$ after beam smearing using different relationships for the velocity dispersions. Shown are the distribution of the $H\alpha$ surface brightness (left), velocity field (middle) and velocity dispersion map (right). In the upper row, we have simply taken the velocity dispersions as estimated from the N-body/SPH simulation, while for the lower row we assumed a relationship between the velocity dispersion and star-formation intensity of the form $\sigma = 140 \sqrt{\Sigma_{\text{SFR}}}$ km s^{-1} . The circle in the upper right of each plot represents the FWHM of the PSF used to make the artificial data set. The scales are in arc seconds. We note that we have scaled the images such that the sizes of these panels and those in Fig. 5 are similar, for ease of direct comparison.

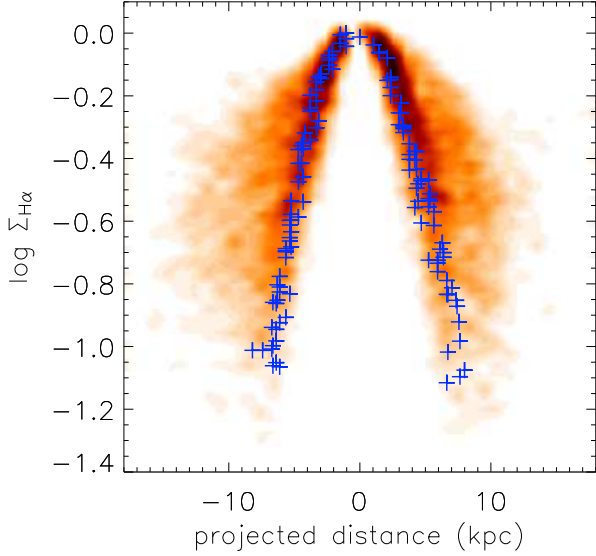


Fig. 7. Comparison of the relative frequency of occurrence of pixel values of normalized per pixel $H\alpha$ surface brightness distributions of the whole sample of galaxies (in shades of red) with superimposed an artificial SINFONI data set constructed from an N-body/SPH simulation (blue crosses). Both observations and simulation follow similar distributions.

of all of this, the general trend for higher star-formation intensity to result in higher dispersion is maintained.

We also halved the signal-to-noise ratio and used the intrinsic rotation speed of the simulated galaxy keeping the inclination angle at 45° . In both cases, the overall trend in the data is maintained and the increase in the scatter in the star-formation intensity-dispersion plane is not significant.

4.4. Are the dispersions related to $H\alpha$ surface brightness?

We now compare the observed trend between star-formation intensity and $H\alpha$ line velocity dispersion with the models we used to make synthetic data sets, including the effects of beam smearing. Fig. 9 shows that the values of the simulated $H\alpha$ line dispersion σ_{sim} are too low to explain the large line widths we generally observe in our sample of galaxies. On the other hand, the simulation using the relationship, $\sigma \propto \Sigma_{\text{SFR}}^{1/2}$, is a good match to the overall distribution of the data. We note that more properly, a constant term should perhaps be included in the relationship, as $\sigma \propto \Sigma_{\text{SFR}}^{1/2} + \text{constant}$, which is both warranted by observations and expected theoretically (Dib et al. 2006). At star formation intensities of order 10^{-4} to $10^{-5} M_{\odot} \text{ yr}^{-1} \text{ kpc}^{-2}$, the observed velocity dispersion of the $H\alpha$ emission line are $\sim 5\text{--}20 \text{ km s}^{-1}$ (Fathi et al. 2007; Erroz-Ferrer et al. 2012). We have chosen to ignore this constant in our analysis for two reasons. First, velocities this small are below the resolution of the SINFONI data. Thus we are unable to probe the characteristics of galaxies with low star formation intensities. Second, the star formation intensities of the galaxies we are observing are several orders of magnitude greater and this including a small constant term would have an insignificant impact on our analysis or conclusions.

Figure 10 displays the differences in the $H\alpha$ velocity as a function of the star-formation intensity distribution for the galaxies in two different redshift regimes, $z < 1.8$ and $z > 2$. The key re-

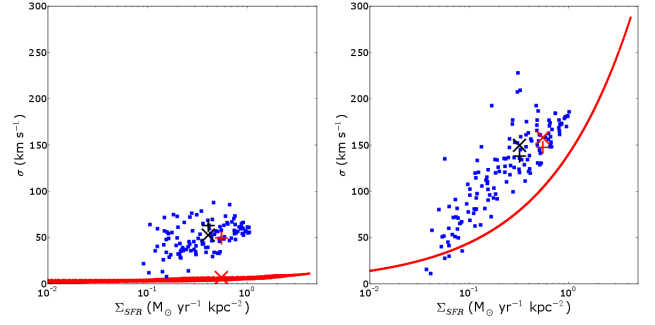


Fig. 8. In our analysis of the impact of beam smearing on the velocity dispersion and star-formation intensity, we adopted two relationships between these two quantities. One taken directly from the simulations (*left panel*), and another where we assumed $\sigma \propto \Sigma_{\text{SFR}}^{1/2}$ (*right panel*). The model velocity dispersions are shown in red (these are not lines but many individual points). We also show the points (blue) after analyzing the artificial data cubes derived from the simulation which include the effects of beam smearing. The red + (red \times) sign indicates the mean star-formation intensity and integrated (original input) velocity dispersion for the intrinsic relation between velocity dispersion and star-formation intensity, while the black + (black \times) sign has the same meaning but now for the beam-smear relationship.

sult is that the data are consistent with a simple scaling between dispersion and star-formation intensity in both samples – however, on average the $z \sim 1.5$ galaxies have lower dispersions and star-formation intensities. Also, the scatter is larger for the lower redshift galaxies, which perhaps indicates that a single relationship of the type $\sigma \propto \sqrt{\Sigma_{\text{SFR}}}$ does not explain all of the trends in the lower-redshift data as well as it does for the higher redshift objects.

At the low end of the star-formation intensity within individual galaxies and over the ensemble of galaxies with lower average star-formation intensities, it is likely that we are overestimating the velocity dispersions, and it could be that the dispersions are becoming roughly constant with radius. We say this, because our artificial model-based data cubes suggest that observed dispersions smaller than $\sim 40\text{--}50 \text{ km s}^{-1}$ are consistent with $\lesssim 10 \text{ km s}^{-1}$, a level at which we simply can no longer differentiate between a model where the line widths are proportional to $\Sigma_{\text{SFR}}^{1/2}$ or one where the line widths are consistent with what is observed in the MW and other nearby galaxies (see, e.g. Wada et al. 2002; Dib et al. 2006; Agertz et al. 2009).

In Figures 10, we plotted the simulated data against the normalized distribution of star formation intensity and velocity dispersion. However, this does not give a sense of the differences between galaxies at different redshifts in their distribution of star formation intensity and velocity dispersion. The distributions of the galaxies in the higher redshift regime are consistent with those of 11 galaxies presented in Lehnert et al. (2009). Quantitatively, the ensemble of galaxies with $z > 1.8$ and $z < 1.8$ have a mean star formation intensity of 0.73 ± 0.09 and $0.16 \pm 0.02 M_{\odot} \text{ yr}^{-1} \text{ kpc}^{-2}$ respectively. Since both samples contain about the same number of galaxies, the width of the distribution of the higher redshift sample is significantly larger and the difference in width between the samples is consistent with Lehnert et al. (2009).

Moreover, correcting individual galaxies in the sample for the average extinction (derived from fitting the spectral energy distribution with stellar population synthesis models;

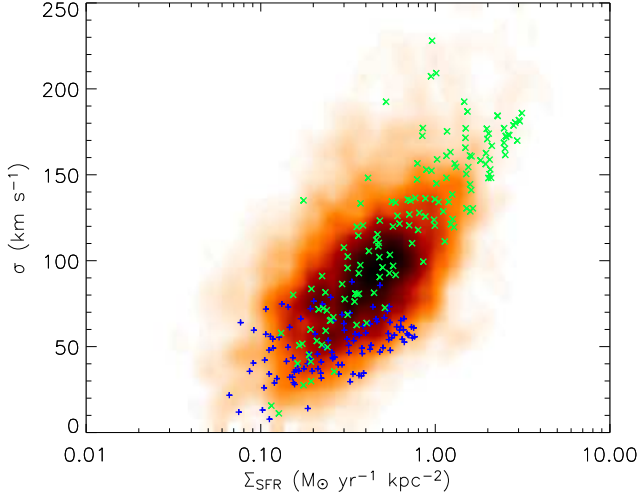


Fig. 9. Normalized 2-dimensional histogram of the frequency of occurrence in the data set of $H\alpha$ line widths as function of star formation rate intensity. The set of points for each galaxy are normalized such that all of the galaxies have the same mean star-formation rate intensity (their distribution of the velocity dispersion in each galaxy is unaffected). The mean value was chosen to match the mean value of the star-formation intensity in the model with $\sigma = (\epsilon \Sigma_{\text{SFR}})^{1/2}$ as indicated by the red + sign in the right panel of Fig. 8 ($\sim 0.5 M_{\odot} \text{ yr}^{-1} \text{ kpc}^{-2}$). As in Fig. 2, the darkest regions represent the highest frequency of occurrence in the data set. The green \times and blue + symbols represent our simulated data after beam smearing, assuming that the two quantities plotted are related as $\sigma = (\epsilon \Sigma_{\text{SFR}})^{1/2}$ and $\sigma = \sigma_{\text{sim}}$, respectively.

Förster Schreiber et al. 2011) does not reduce the scatter among them.

4.5. The equivalence of integrated and spatially resolved measurements

So far, we have studied the spatially resolved relationship between the $H\alpha$ velocity dispersion and the star-formation intensity as probed by the $H\alpha$ emission. In Le Tiran et al. (2011a), we argued that the relationship between the integrated $H\alpha$ luminosity (or equivalently the total star-formation rate) and surface brightness-weighted mean dispersion of whole galaxies reveals the same underlying physical mechanism as the spatially resolved measurements – namely, that the intense star-formation is responsible for the dynamics of the warm ionized medium as probed through the $H\alpha$ recombination line (see also Green et al. 2010).

To further investigate this relationship, we have tested the idea that the intense star-formation in these galaxies can even explain the integrated measurements of the total star-formation rate and the integrated velocity dispersion. This is important: if we can show that also these integrated measurements reveal this underlying relationship, then a greater wealth of data become available for analysis, since slit spectra are more commonly available than integral field spectra.

We first note that we find little difference in velocity dispersion for whole galaxies if we simply sum up the $H\alpha$ emission pixel-by-pixel and estimate their integrated dispersion or if we weigh each measurement by surface brightness (or signal-to-noise). The difference between both methods is only about 15

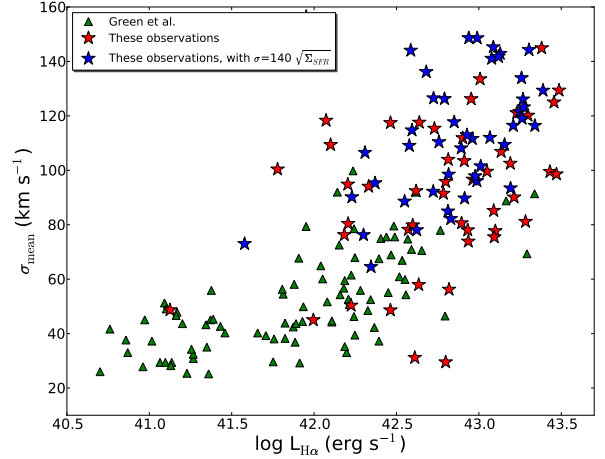


Fig. 11. Mean $H\alpha$ line velocity dispersion, σ_{mean} (in km s^{-1}), versus total $H\alpha$ luminosity (in erg s^{-1}) for different samples of local and high redshift galaxies. Local galaxies (green triangles) are taken from Green et al. (2010) and the model results for our sample are represented by red and blue stars. The blue stars show the results where we assign to each pixel in a galaxy an $H\alpha$ surface brightness based on the model relationship, $\sigma = 140 \sqrt{\Sigma_{\text{SFR}}} \text{ km s}^{-1}$ and use the observed local $H\alpha$ velocity dispersion. We then estimate the total $H\alpha$ luminosity by summing up the predicted pixel-by-pixel surface brightnesses, and estimate σ_{mean} by weighting the pixel-by-pixel velocity dispersion measurements by the $H\alpha$ surface brightnesses derived from the model.

km s^{-1} , where flux weighting tends to give a lower value and a scatter of about 15 km s^{-1} . So compared to the mean integrated velocity dispersion of our sample, this represents a systematic offset of only about 10% (Le Tiran et al. 2011a).

To further test the relevance of a relationship of the form, $\sigma = (\epsilon \Sigma_{\text{SFR}})^{1/2}$, where ϵ is the efficiency at which the mechanical energy from a star-formation intensity Σ_{SFR} is converted into turbulence and bulk flows in the interstellar medium, we applied it to the spatially resolved dispersion measurements, to estimate integrated quantities. Specifically, we used the spatially resolved, pixel-by-pixel $H\alpha$ line velocity dispersion measurements to estimate the $H\alpha$ surface brightness of each pixel. We then used these surface brightness estimates as weights when combining the individual pixel-by-pixel velocity dispersions, to estimate the integrated mean dispersion in $H\alpha$, σ_{mean} . We summed these estimated surface brightness values to estimate the integrated $H\alpha$ fluxes and then converted these to total luminosities using our adopted cosmology. The results of this analysis show that we can reproduce the actual measurements reasonably well considering the crudeness of the model and that we only considered one coupling efficiency (Fig. 11). So not only does this simple scaling relationship reproduce the spatially resolved measurements, but it can also reasonably reproduce the integrated measurements. Apparently, unlike in many models of the ISM, the observed velocity dispersion of the warm ionized medium does increase with increasing star-formation intensity and rate (Dib et al. 2006; Ostriker & Shetty 2011).

5. Discussion

Figure 12 shows that $[\text{NII}]/H\alpha$ ratios are not arbitrary, but scale with $H\alpha$ surface brightness. This has already been noted by

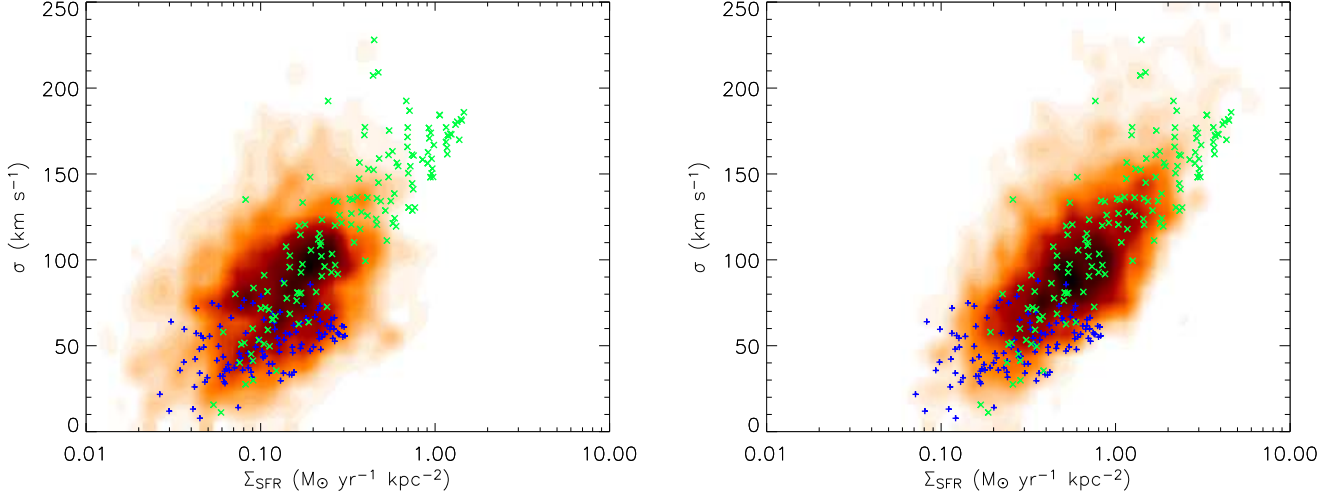


Fig. 10. Plots of the normalized frequency of occurrence of $H\alpha$ velocity dispersion versus star-formation intensity in two redshift bins, $z < 1.8$ (left) and $z > 2$ (right) (cf. Fig. 9 for the whole sample). The normalizations are different from that used in Fig. 9 and in the left and right panels. For both sub-samples, the average star-formation intensity of each galaxy was shifted to the average of its ensemble of galaxies ($0.16 M_{\odot} \text{ yr}^{-1} \text{ kpc}^{-2}$ for $z < 1.8$ and $0.73 M_{\odot} \text{ yr}^{-1} \text{ kpc}^{-2}$ for $z > 2$). Note that the two sub-samples tend to sample different ranges in both velocity dispersion and star-formation intensity. The green \times and blue $+$ symbols represent our simulated data after beam smearing, assuming that the two quantities plotted are related as $\sigma = (\epsilon \Sigma_{\text{SFR}})^{1/2} \text{ km s}^{-1}$ and $\sigma = \sigma_{\text{sim}}$, respectively. The green and blue model points have been shifted to overlap with the data (the location of the modeled points along the axis of Σ_{SFR} is set by the coupling efficiency of the mechanical energy output of young stars to the ISM).

Lehnert et al. (2009) and is confirmed with our new, larger sample. The emission line ratios and $H\alpha$ surface brightnesses are related to the gas pressure, column density, intensity of the radiation field and the number of line-emitting regions along the line of sight within each beam. New, compared to our previous analysis of this relationship, is that our expanded sample includes galaxies at lower redshift, which in turn will allow us to probe pressures, column densities and radiation fields in galaxies with less extreme $H\alpha$ surface brightnesses.

Measurements of the $[\text{SII}]$ doublet ratio in individual galaxies in a sub-sample of this sample (Lehnert et al. 2009) and through a stacking analysis of this sample (Le Tiran et al. 2011b), suggest that the typical densities of the warm ionized gas are $n_e \sim 10$ s to $\sim 500 \text{ cm}^{-3}$. To compare these estimates, we ran a suite of photoionization models using version 08.01 of the Cloudy code (Ferland et al. 1998) to show the relationship between the $[\text{NII}]\lambda 6583/H\alpha$ line ratio and the $H\alpha$ surface brightness as a function of the hydrogen internal pressure, column density and ionization parameters for a single ionized cloud (see Lehnert et al. 2009). Unfortunately, the interpretation of such modeling is ambiguous due to the degeneracy between surface brightness, line ratio and the number of individual emission line regions per large physical beam of our observations. Given the crude sampling of our data, it is likely that the densities are lower than predicted by a single cloud model, as would be the ionization parameters. Therefore, for both the higher and lower redshift data sets, the likely densities are certainly $< 1000 \text{ cm}^{-3}$ but generally larger than a few times 10 cm^{-3} and are consistent with estimates of the electron density directly measured from the $[\text{SII}]$ doublet ratio in individual galaxies and a stacking analysis.

There is an interesting difference in the regions occupied in the $[\text{NII}]\lambda 6583/H\alpha$ versus $H\alpha$ surface brightness plane by galaxies at $z < 1.8$ and $z > 2$. Taken at face value, it would suggest we are probing less dense gas in the lower redshift galaxies. However, this is undoubtedly due to probing lower surface brightness gas, related to the strong influence of surface brightness dimming, which allows us to probe the very diffuse, perhaps even shock heated, gas in the lower redshift sample (the regions with relatively low surface brightness and high ratios of $[\text{NII}]\lambda 6583/H\alpha$ in Fig. 12 likely require a contribution to their ionization from shocks). This effect is observational, rather than evolutionary. A complete census of both redshift regimes would be necessary to show that the average pressure or number of overlapping emission line regions (i.e. thickness) in the warm ionized media of galaxies is declining with redshift.

The thermal pressures estimated from the electron densities are much higher than in the disk of our Milky Way or other nearby normal galaxies. The hydrostatic mid-plane pressure in the MW is about $10^{3.3-4.3} \text{ K cm}^{-3}$, while for other local spirals it can amount to about 10^6 K cm^{-3} , though it is typically about $10^{4.6} \text{ K cm}^{-3}$ (Blitz & Rosolowsky 2006, and references therein). In the nuclear regions of local starburst galaxies, thermal pressures estimated from the $[\text{SII}]$ doublet ratio are typically about $10^{6-7} \text{ K cm}^{-3}$ (Lehnert & Heckman 1996). The pressures we estimated from the photo-ionization models are consistent with those of nearby intensely star-forming galaxies (Heckman et al. 1990; Lehnert & Heckman 1996; Wang et al. 1998) and measurements of density-sensitive lines at high redshift ($[\text{SII}]$ doublet ratio; Le Tiran et al. 2011b; Lehnert et al. 2009; Nesvadba et al. 2007).

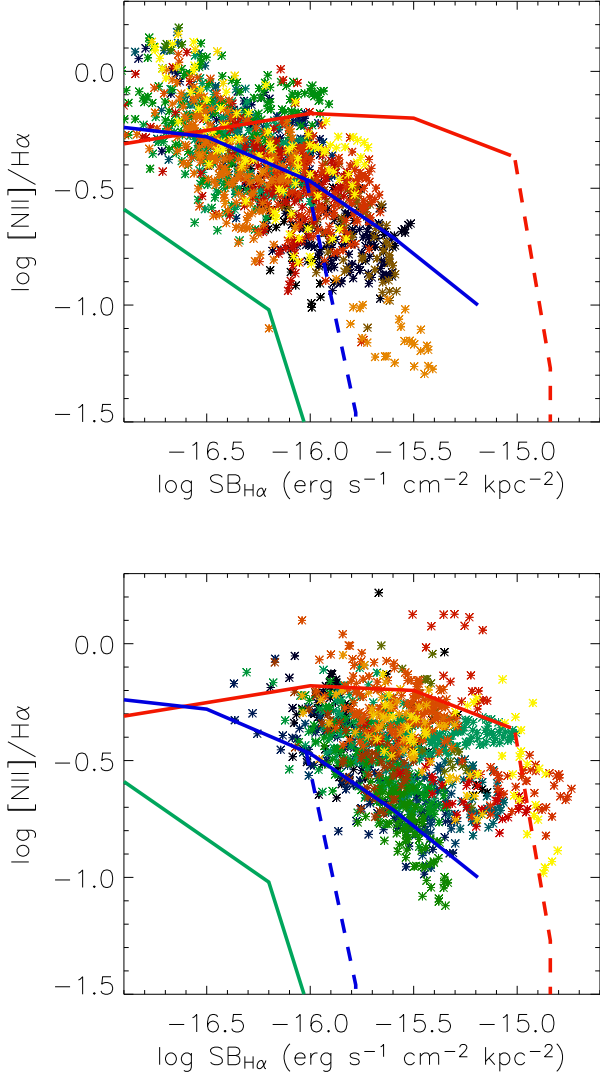


Fig. 12. $H\alpha$ surface brightness (corrected for cosmological surface brightness dimming) versus the logarithm of the $[\text{NII}]\lambda 6583/H\alpha$ line ratio. The galaxies have been separated into two redshift bins: $z < 1.8$ (top) and $z > 2$ (bottom). The lines represent results for photo-ionization modeling (see text for details) for 6 sets of conditions: a range of hydrogen densities, $\log n_H$ (cm^{-3}) = 1 (in green), 2 (blue) and 3 (red), and of column densities, $\log N_H$ (cm^{-2}) = 21 (solid lines) and 20 (dashed lines). The ionization parameters range from $\log U = -5$ to -1 (increasing from left to right along the lines, meaning low ionization parameters have relatively high $\log [\text{NII}]/H\alpha$ and low $H\alpha$ surface brightnesses). At low ionization parameters the solid and dashed lines for the column densities overlap until the lower column density cloud becomes density bounded, at which point the models reach very low ratios of $[\text{NII}]\lambda 6583/H\alpha$ (as shown by the sharply dropping dotted lines). For clarity, we only show the $\log N_H$ (cm^{-2}) = 21 and $\log n_H$ (cm^{-3}) = 3 line until $\log U = -3$ and for $\log N_H$ (cm^{-2}) = 21 and $\log n_H$ (cm^{-3}) = 2 until $\log U = -2$.

By comparing these thermal pressures in the WIM to that generated by the radiation pressure of the ionizing radiation field, it is possible to constrain the general distribution of the WIM (Krumholz & Matzner 2009). Our optical line ratios sug-

gest that the gas is predominately photoionized by massive stars (Lehnert et al. 2009). To estimate the impact of radiation pressure on an ionized fluid, it is appropriate to only consider the ionizing radiation. We can use the ionization parameter to gauge the relative contribution of radiation pressure to the thermal pressure of the WIM. Simple scaling of the definition of the ionization parameter suggests $P_{\text{rad}}/P_{\text{thermal}} = 2.5 \times 10^{-2} U$ ($\langle h\nu \rangle / 18 \text{ eV} / k(T/10^4 \text{ K})$ for $T = 10^4 \text{ K}$ and $\langle h\nu \rangle = 18 \text{ eV}$, where $\langle h\nu \rangle$ is the average energy of ionizing photons and k is the Boltzmann constant. Since the ionization parameter is always less than $\log U = -1.6$ (and mostly $\lesssim -3$), the radiation pressure is lower than the thermal gas pressure throughout the nebulae. Finding that the thermal pressure dominates the radiation pressure and that the ionization parameters are relatively low, suggests that the WIM is widely distributed over the volume of the ISM in our sample of galaxies, truly part of the general interstellar medium, and not simply near or directly associated with the star forming clumps or regions (see Krumholz & Matzner 2009, for a detailed discussion of this point). This point is crucial for our subsequent analysis as it suggests that the WIM is a tracer of the dynamics of the general ISM in distant galaxies and not merely of the $H\text{II}$ regions or clumps.

Other models or relationships have been proposed to explain the high dispersion in the warm ionized gas that are directly related to the ionization state of the gas. Wisnioski et al. (2012) and Swinbank et al. (2012) propose that the relationship between star formation intensity and velocity dispersion can be explained by a relation between the luminosity of a Hydrogen recombination line (e.g. $H\beta$) and the gas velocity dispersion, as observed in local $H\text{II}$ regions (e.g. Terlevich & Melnick 1981). The sizes of local $H\text{II}$ regions and the relationship between line luminosity and velocity dispersion can be understood simply if the gas within the $H\text{II}$ regions is virialized (Terlevich & Melnick 1981). In such a hypothesis, the line widths are mainly due to virial motions, implies that the warm ionized medium is in close proximity to the star forming clumps (within the gravitational sphere of influence). Nearby HII regions, for which such a relation is appropriate, generally show ionization parameters that are high, $\log U \approx -1$ to -2 (e.g. López-Hernández et al. 2013), but our analysis suggests that distant galaxies generally have much lower ionization parameters, implying that their emission line gas luminosity is dominated by more widely distributed gas and not directly associated with the clumps.

5.1. Source of the pressure in the WIM

What are the sources of pressure in these distant galaxies? Is the pressure generated by the thermalization of the collective mechanical energy output of massive stars through the thermalization of stellar winds and supernova explosions? Observations of nearby galaxies suggest that the low ionization line emitting region is approximately in pressure equilibrium with the X-ray emitting plasma, with thermal pressures in the range 10^{-9} to $10^{-10} \text{ dyne cm}^{-2}$ (e.g. Heckman et al. 1990; Moran et al. 1999; Westmoquette et al. 2007; Strickland & Heckman 2009). Similar pressures are found in models using typical initial conditions expected for galaxies exhibiting outflows (e.g. Suchkov et al. 1996). If these two phases are in equilibrium then we can use a simple model to estimate the pressures in the hot X-ray emitting plasma to see if it agrees with our estimates of the thermal pressures (densities) in the warm ionized media in distant galaxies.

Strickland & Heckman (2009) has shown that the simple analytic expressions of Chevalier & Clegg (1985) for the pressure,

temperature and velocity of outflows driven by the intense energy injection from young massive stars agree with hydrodynamical simulations. Adopting and scaling these simple relations from Chevalier & Clegg (1985) we estimate the central pressure in a starburst region as $P_c = 3.5 \times 10^{-10} (\zeta M_{0.26})^{1/2} (\epsilon_{\text{thermal}} \dot{E}_{41.9})^{1/2} R_{\text{SB},350}^2 \Omega$ dyne cm^{-2} , where ζ is the mass-loading factor, $M_{0.26}$ is the mass return rate in units of $0.26 M_{\odot} \text{yr}^{-1}$, $\epsilon_{\text{thermal}}$ is the thermalization efficiency of the stellar winds and supernovae, $\dot{E}_{41.9}$ is the energy injection rate in units of 7.4×10^{41} erg s^{-1} , $R_{\text{SB},350}$ is the radius of the starburst in units of 350 pc and Ω is the opening angle of the outflow in sr. The adopted scalings for the mass and energy injection rates from massive stars are appropriate for a star formation rate of $1 M_{\odot} \text{yr}^{-1}$ (Leitherer et al. 1999) within a radius consistent with clump sizes and $\text{H}\alpha$ disk thicknesses in high redshift galaxies (Förster Schreiber et al. 2011; Epinat et al. 2012). For the radius scaling, see Strickland & Heckman (2009).

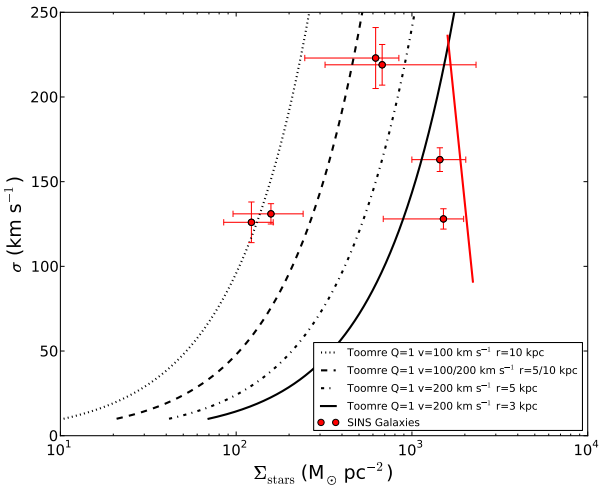


Fig. 13. $\text{H}\alpha$ velocity dispersion, σ as function of stellar mass surface density, Σ_{stars} ($M_{\odot} \text{pc}^{-2}$). The lines represent the Toomre criterion $Q=1$ for two rotation speeds ($v=100$ or 200 km s^{-1}) and three radii ($r=3, 5, 10 \text{ kpc}$), as indicated in the legend. These values span the range of radii and velocity shears observed in these galaxies (Förster Schreiber et al. 2006, 2009). The stellar mass surface densities (red dots) are estimates within one effective radius for 6 galaxies in our sample with NICMOS images (see text). The red solid line shows the relationship between central velocity dispersion and stellar mass surface density for local early-type galaxies (Shen et al. 2003; Taylor et al. 2010).

Reasonable assumptions for the thermalization efficiency, mass loading factor, and mass and energy injection rates, result in pressures of 10^{-9} to 10^{-10} dyne cm^{-2} in our galaxies, similar to what is estimated for nearby starburst galaxies. This simple modeling suggests that the hot plasma generated by the thermalization of the mechanical energy output of young stars can generate sufficient pressure to approximately match our estimates for the thermal pressure in the warm ionized medium.

One of the assumptions that is needed for the model to be appropriate is that the energy injection rate is approximately constant over an outflow timescale (e.g. Chevalier & Clegg 1985; Suchkov et al. 1996; Strickland & Heckman 2009). This has been shown to be true for local starbursts (e.g. Heckman et al. 1990; Lehnert et al. 1999). While we do not know the outflow

timescale of the distant galaxies, since their star-formation intensities are similar to nearby starburst galaxies (see discussion in Lehnert et al. 2009), it is logical to assume their outflow timescales would be similar (10s Myr or less). Distant galaxies similar to the ones observed here (e.g. Erb et al. 2006; Förster Schreiber et al. 2011) have star formation timescales of ≈ 100 s Myrs and are likely much longer than the outflow timescales. A reasonable assumption is that the energy injection rate is approximately constant in distant galaxies as it appears to be in nearby starbursts and thus the model of Chevalier & Clegg (1985) is an appropriate approximation for estimating the pressures (see also Strickland & Heckman 2009, for a discussion).

5.2. Mass and energy flow?

The aforementioned rough equality of the thermal pressure in the two ISM phases, the hot 10^7 – 10^8 K plasma and the 10^4 K warm ionized medium, is important. It may imply that the mechanical energy injected into the ISM of the galaxy couples efficiently with the recombining gas and perhaps drive a mass and energy flow from the WIM to the cold neutral and molecular medium (Guillard et al. 2009, 2010). The recombining gas is unstable at the pressures we observe and will quickly cool, collapse and become part of the cold neutral medium, CNM (Wolfire et al. 1995). Since this is expected to happen quickly this would imply that the CNM acquires the relative kinematics of the WIM (Guillard et al. 2012). If the gas is dusty, this recombining gas will rapidly turn molecular since the H_2 formation time scales on dust grains is much shorter than the expected dynamical time scales of the recombining, cooling and collapsing clouds (Guillard et al. 2009). The formation of gravitationally bound clouds releases gravitational energy as turbulence into the molecular gas.

This picture links the energy input from intense star formation to energy dissipation, the formation of molecular gas and star formation. Thus not only is this a flow of mass and energy but also one of kinetic energy, which will not only contribute to the turbulent energy of the molecular gas but also serve to balance dissipation. Of course, it is not a simple one-directional flow, but a cycle or feedback loops where individual molecular clouds may form stars when they become self gravitating, or simply be heated and destroyed. Naturally, because all the timescales in the cycle are relatively short, $\lesssim 10$ Myrs, the ISM will be in a dynamical equilibrium. The components of the ISM should not be viewed as single, isolated components but rather as an intricate balance whose relative mass flow rates are determined by a competition between the heating and cooling rates as well as the outflow rate due to starburst driven winds and the in-fall rate due to the cosmological accretion of gas through cooling gas and mergers.

One of the conditions that must be met in such a picture is that the mass deposition rate of the WIM should be more than sufficient to fuel star formation, or $\dot{M}_{\text{SF}} \lesssim \epsilon_{\text{starform}} \dot{M}_{\text{HII}}$, where $\epsilon_{\text{starform}}$ is the efficiency of star formation. The recombination rate of the $\text{H}\alpha$ emitting gas is given by simple ionization balance, $\dot{M}_{\text{HII}} = 1.9 \times 10^5 L_{\text{H}\alpha,43} M_{\odot} \text{yr}^{-1}$. The star formation rates in these galaxies are ~ 10 – $300 M_{\odot} \text{yr}^{-1}$ and thus the WIM recombination rates can supply the gas for star formation as long as the star formation efficiency is $\geq 0.1\%$. For a reasonable $\epsilon_{\text{starform}}$ only a small fraction, a few to about 10 percent, of the recombining gas would then be necessary to fuel this cycle. So at least in terms of mass flow rates, there is sufficient mass in the warm ionized medium to plausibly sustain such a cycle.

Of course, for the energy injection to be effective in regulating star formation, as we have hypothesized, it should drive the galaxy towards the line of Toomre disk stability, $Q\sim 1$. This occurs if the star formation can inject sufficient turbulence to roughly balance gravitational collapse and hydrostatic pressure.

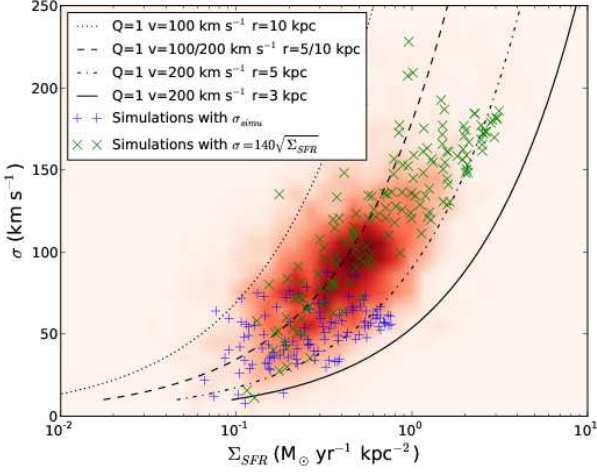


Fig. 14. $H\alpha$ velocity dispersion, σ , as function of the star formation intensity, Σ_{SFR} ($M_{\odot} \text{ yr}^{-1} \text{ kpc}^{-2}$). The lines represent the Toomre criterion for gas, assuming both $Q=1$ and that the Schmidt-Kennicutt relation is appropriate for a variety of rotation speeds and radii, as in Fig. 13 and as indicated in the legend (see text for details). The underlying display of the normalized data (shown in various shades of red) is the same as in Fig. 9 (see that figure and text for details).

While the WIM traces the overall dynamics of the ISM (see beginning of § 5), its contribution to the turbulent pressure is negligible. It is given by $P_{\text{gas,turb}} = \langle \rho_{\text{gas}} \rangle \sigma_{\text{gas}}^2$ where $\langle \rho_{\text{gas}} \rangle$ is the volumeweighted mean density ($=\rho_{\text{phase}} f_{V,\text{phase}}$, where ρ_{phase} is the intrinsic density and $f_{V,\text{phase}}$ the volume filling factor of the ISM phase). The total turbulent pressure is actually the sum of those of all individual ISM phases, but we have suppressed the summation for clarity. The $H\alpha$ emitting gas likely does not contribute significantly to the total turbulent pressure. Assuming simple case B recombination, $T_e=10^4$ K and equality of proton and electron densities, we can crudely calculate the emitting volume needed to supply the $H\alpha$ luminosity compared to the volume over which it is observed. The volume filling factor of the recombining gas is $ff_{V,WIM} \sim V_{\text{em}}/V_n = 4 \times 10^{-5} L_{H\alpha,43} n_{e,300}^2 V_{n,100}^{-1}$, where V_{em} is the emitting volume, $V_{n,100}$ is the actual ISM volume in units of 100 kpc^3 (the typical isophotal area is 100 kpc^2 and we assumed a disk thickness of 1 kpc), $L_{H\alpha,43}$ is the $H\alpha$ luminosity in units of $10^{43} \text{ erg s}^{-1}$ and $n_{e,300}$ is the electron density in units of 300 cm^{-3} . The filling factor of the recombining gas is $\sim 10^{-6}$.

The most significant contribution to the total turbulent pressure is likely from the cold neutral and molecular medium. We can estimate the density of the dense molecular gas using observations of distant galaxies with star formation rates and general properties similar to ours. H_2 gas mass surface density measurements are available for galaxies similar to those studied here ($z\sim 1$ and 2; Daddi et al. 2010; Aravena et al. 2010; Dannerbauer et al. 2009; Tacconi et al. 2010; Combes et al. 2011) which suggest that at $z\sim 2$ the mean value is about 500

$M_{\odot} \text{ pc}^{-2}$ and that total gas fractions $\sim 30\text{--}50\%$ (Daddi et al. 2010; Tacconi et al. 2010). The volume weighted H_2 gas density, $\langle n_{\text{H}_2} \rangle = \Sigma_{\text{gas}}/H m_{\text{H}_2} = 10.2 \Sigma_{\text{gas},500}/H_{1\text{kpc}}$, where $\Sigma_{\text{gas},500}$ is the gas mass surface density in units of $500 M_{\odot} \text{ pc}^{-2}$ and $H_{1\text{kpc}}$ is the thickness of the gas layer in units of 1 kpc. This implies that $P_{\text{turb,mol}} = 3 \times 10^{-9} \langle \rho_{\text{gas},10} \rangle > \sigma_{\text{H}_2,100}^2$, where $\langle \rho_{\text{H}_2,10} \rangle$ is the H_2 volume weighted particle density in units of 10 cm^{-3} and $\sigma_{\text{H}_2,100}$ is in units of 100 km s^{-1} . These estimates suggest that the turbulent pressure in the molecular gas may be high (Swinbank et al. 2011).

For a galaxy to lie near the line of stability, $Q=1$, the pressure due to gravity and that due to turbulence should be roughly equal. To estimate the pressure due to gravity we will assume hydrostatic equilibrium, which is obviously an oversimplification. However, for the present analysis, we are concerning ourselves with globally averaged estimates, suggesting that hydrostatic equilibrium is a reasonable assumption. It is impossible to get direct estimates for the hydrostatic gas pressures for our sample of galaxies as stellar mass surface densities are available for only a few objects (Förster Schreiber et al. 2011). As with the estimates of the volume-weighted gas mass densities, we will have to rely on results from similar samples of distant galaxies, which find stellar mass surface densities of $100\text{--}2000 M_{\odot} \text{ pc}^{-2}$ (e.g. Barden et al. 2005; Yuma et al. 2011; Förster Schreiber et al. 2011). The hydrostatic pressure scales as $P_{\text{gas,hydro}} = 7 \times 10^{-10} \Sigma_{\text{gas},500} \Sigma_{\text{total},1500} \text{ dyne cm}^{-2}$, where $\Sigma_{\text{gas},500}$ is the gas mass surface density in units of $500 M_{\odot} \text{ pc}^{-2}$ and $\Sigma_{\text{total},1500}$ is the stellar mass surface density in units of $1500 M_{\odot} \text{ pc}^{-2}$. For this estimate of the hydrostatic pressure, we have assumed that the velocity dispersion of the gas and stars are equal, which is consistent with our general underlying hypothesis that the velocity dispersions of the warm ionized and the cold molecular ISM phases are similar. However, this is not a tight constraint as lowering the dispersion in the gas would lower the turbulent pressure as well as the hydrostatic pressure for a fixed stellar velocity dispersion. The estimated ranges of gas fraction and stellar surface densities for $z\sim 2$ galaxies (Daddi et al. 2010; Tacconi et al. 2010) suggests hydrostatic pressures of $P_{\text{gas,hydro}} \sim 10^{-9}$ to $10^{-10} \text{ dyne cm}^{-2}$. Thus it appears that the hydrostatic pressure and the turbulent pressure in the molecular gas are similar if the molecular gas has kinematics similar to that of the WIM.

5.3. Surface densities and the Toomre Q parameter

We have argued that if the turbulence in the molecular gas were similar to that of the WIM, then the distant galaxies should lie near the line of stability. We proposed a qualitative scenario where the kinematics of the WIM may be roughly captured by the cold molecular gas and thus lead to high turbulence. Furthermore, we suggested that these intensities can be understood in terms of self-regulation (Silk 1997, 2001). Such self-regulation would reveal itself through mass surface densities in the galaxies consistent with $Q=1$.

Krumholz & Dekel (2010) favor disk instabilities as the source of the high velocity dispersion in distant galaxies with spatially-resolved kinematics and line emission (see also, e.g. Cacciato et al. 2012). Their argument is that this is the simplest explanation, because it is based on the Toomre instability parameter, $Q = \kappa \sigma / \pi G \Sigma$, where κ is the epicyclic frequency (which in our subsequent analysis we have taken to be $2^{1/2} v/r$, where v is the rotation speed and r is the radius) and Σ is the mass surface density of stars or gas (Wang & Silk 1994; Romeo & Wiegert

2011). They suggest that the high velocity dispersions are a natural result of the need to keep the star-formation intense, which implies that $Q \sim 1$. The results given above suggest perhaps that the star-formation itself may also lead to $Q \sim 1$ (see also Ostriker & Shetty 2011). Combining the Schmidt-Kennicutt relation with the Toomre instability criterion, $Q=1$, suggests that $\sigma \propto \Sigma_{\text{SFR}}^{0.7}$. This is similar enough to our suggested relationship as to be indistinguishable (Wisnioski et al. 2012; Swinbank et al. 2012). Swinbank et al. (2012) show that assuming a marginally stable Toomre disk combined with relationships for the largest unstable fluctuations in disks and a Jeans relation for the growth of unstable modes, can lead to insights into why disks at high redshift may have high dispersions, why clumps have high mass surface densities, why their masses in disk galaxies decline with redshift and why their mass distributions have exponential cut-offs. However, such a solution does not explain how the observed high dispersions are maintained. This either requires a long dissipation time or a large source of mechanical energy (Mac Low 1999; Ostriker & Shetty 2011). What maintains the instability such that $Q \sim 1$? We suggest it is the star-formation itself that maintains the necessary dispersion in the gas phase, as we will now argue.

The Toomre parameter for the stellar population is $Q = \kappa \sigma / \pi G \Sigma_{\text{stars}}$, where Σ_{stars} is the mass surface density of stars. For the galaxies we have presented here, the velocity shears are of-order 100-200 km s^{-1} (Förster Schreiber et al. 2006, 2009) and the radii are about a few to 10 kpc (Förster Schreiber et al. 2011). The mass surface density, $\Sigma_{\text{stars}} = M_{\text{stars}} / 2\pi(b/a)r_e^2$, where M_{stars} is the total stellar mass, b/a is the minor-to-major axis ratio and r_e is the effective radius. Using NICMOS and other imaging data of 6 galaxies in our sample, we have made crude estimates of stellar mass surface densities using the results from Förster Schreiber et al. (2011). We find that the mass surface densities within one effective radius are $\sim 100\text{-}1500 M_{\odot} \text{ kpc}^{-2}$. Assuming $Q=1$, we can relate the velocity dispersion to the mass surface density and it appears that the estimated mass surface densities are consistent with $Q=1$ (Fig. 13).

Without considering the effects of beam smearing, this simple relation is actually also roughly consistent with our data on the emission line properties, as we can demonstrate rather simply: if we assume $Q=1$ for the gas, and adopt the Schmidt-Kennicutt relation (Kennicutt 1998) between star formation intensity and gas surface density, we find the relation, $\sigma = (\pi G Q / \kappa) (\Sigma_{\text{SFR}} / 2.5 \times 10^{-4})^{0.7}$. For a variety of rotation speeds and disk radii, we find general consistency with our data (Fig. 14). Of course these estimates are crude and could be fortuitous but they do lend additional weight to our overall arguments. We have not used the generalized (effective) Toomre criterion, $1/Q_{\text{eff}} = 1/Q_{\text{gas}} + 1/Q_{\text{stars}}$ (Wang & Silk 1994; Jog 1996; Romeo & Wiegert 2011) because the crudeness of our analysis does not warrant this additional complication. However, since this is a relatively small change in the adopted Q , it will make little difference to our conclusions which is that the galaxies generally lie near the line of stability.

5.4. Toomre-stability of star-forming high- z disks

Can we make a self-consistent model whereby intense star formation is responsible for driving high turbulence and pushing the ISM in distant galaxies towards the line of stability? Elmegreen & Burkert (2010) developed an analytical model to follow the evolution of gravitational instabilities and star formation in disk galaxies that are built from rapid gas accretion at high, constant rates. The energy of the accretion is balanced

by the dissipation rate and loss of energy due to star formation. The accretion rate is defined by accreting half of a fiducial mass scaling in one dynamical (orbital) time (about 280 Myrs, Elmegreen & Burkert 2010). Star formation only serves as an energy sink in their formalism, to account for gas lost to the ISM because it is bound in stars, but they do not include the energy return from young stars into the ISM in a self-consistent way. In their model, turbulent velocities drop to very low values well before stellar-to-gas mass ratios reach observed values. To overcome this, they force turbulent velocities, σ , to have values consistent with $Q=1$. They find that ultimately the disk reaches an equilibrium where $\dot{M}_{\text{accretion}} = \dot{M}_{\text{star-formation}}$.

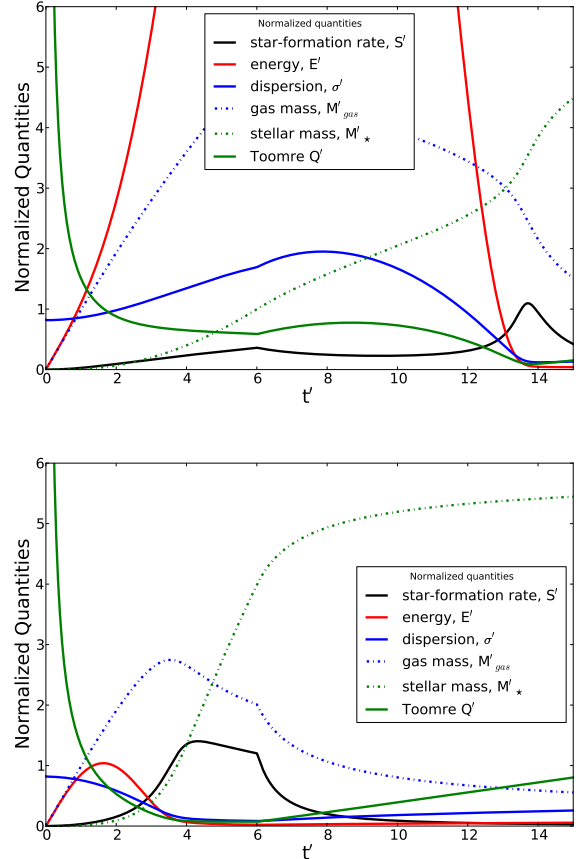


Fig. 15. Six normalized quantities (see legend) as a function of time, where $t/t' = 90$ Myrs or about $1/3$ of a dynamical time of the potential. To limit the total mass so that it does not become too large compared to the observations, the accretion ended at $t'=6$ (about 540 Myrs or two dynamical times). The top panel is for a relatively high assumed efficiency of coupling of the mechanical energy output of the stellar population to the ISM (12%), whereas the bottom panel is for a relatively low coupling efficiency (5%). The scalings for these normalized quantities are provided in the text (see Elmegreen & Burkert 2010).

We will now extend their model to include the effects of the energy release of star formation. This is necessary if we want to investigate how star formation is regulated in galaxies whose evolution is not only driven by accretion and dissipation of turbulent energy, but where star formation contributes significantly to the gas energetics, as indicated by our observational finding that star formation produces pressures similar to the mid-plane

pressure of the disk. In our model, accretion, dissipation and the energy released by star formation together set Q . Including star-formation feedback in this way is one significant difference to the model of Elmegreen & Burkert (2010). The other is that we allow for a cut-off in the gas accretion at some point in the evolution. Some cut-off or severe reduction in the initial high rates of gas supply must have occurred to produce galaxies with masses similar to those generally observed at high redshift. This is not merely an academic issue either. It is often argued that the star formation rate and the gas accretion must be equal, and at the high star formation rates observed in $z \sim 2$ galaxies, the star formation time is a few 100 Myr to 1 Gyr. To account for the energy from star formation, we have modified equation (11) from Elmegreen & Burkert (2010) as follows:

$$\frac{dE'}{dt'} = 1 - M'_{\text{disk}}(E'M'_{\text{gas}})^{1/2} - S'E'/M'_{\text{gas}} + \epsilon_{\text{SF}}E_{\text{SF}}S'M'_{\text{gas}}{}^{3/2}E'^{1/2} \quad (1)$$

where E' , M'_{disk} , M'_{gas} , and S' are the scaled energy, disk mass, gas mass and star-formation rate, respectively (see Elmegreen & Burkert 2010, for details). The first 3 terms are straight from Elmegreen & Burkert (2010). The first term is constant, because for simplicity we assume a constant potential, and it is unity, because the energy is normalized relative to the total accretion energy, which is extracted from the potential. The second term quantifies the turbulent dissipation. The dissipation rate is $E\sigma/H$, where E is the total energy, σ is the turbulent velocity and H is the scale height of the disk, which is determined by a competition between the turbulent energy and the gravitational force due to the total mass surface density, i.e., $H = \sigma^2/\pi G \Sigma_{\text{disk}}$. The third term is the energy that is lost to the ISM when stars form. Adding a time dependence to the potential is quite straight-forward and we have conducted both a time independent and time dependent analysis. To these first three terms from Elmegreen & Burkert (2010) we have added another term to incorporate the energy injection rate from star formation, $\epsilon_{\text{SF}}E_{\text{SF}}S'M'_{\text{gas}}{}^{3/2}E'^{1/2}$, where ϵ_{SF} is the coupling efficiency of the mechanical energy to the interstellar medium of the galaxy and E_{SF} is the rate at which energy is ejected per unit of star formation. The whole equation is normalized such that the accretion energy is one. In addition, other than the parameters already mentioned, other key parameters in determining the evolution of this simple model are the star formation efficiency, the gas accretion rate, the fraction of the accretion energy that couples to the kinematics of the ISM, the fraction of mechanical energy produced by young massive stars that cycles back into the ISM and the dissipation timescale. For these parameters, we adopted the values from Elmegreen & Burkert (2010), although we allowed for a star formation efficiency of 3% in the models instead of 1% they adopted. The fraction of energy produced by massive stars that dynamically coupled to the ISM was a free parameter, which we would like to constrain, and the dissipation timescale was determined by the parameters of the model, as just discussed.

The scalings within this model are quite important. Using the estimates of the mechanical energy per unit star formation (Leitherer et al. 1999) and a rotation speed of 220 km s^{-1} (which sets the potential energy of the galaxy from which the accretion energy is extracted), we estimate that the mechanical energy injected into the ISM by stars is several 100 times greater than that generated by accretion. Also the time scale for star formation is much shorter than that for accretion. Thus star formation can play an important role in injecting energy into the gas and perhaps even pushing disks towards marginal stability against star formation ($Q \sim 1$). The scalings for the original model (taken

from Elmegreen & Burkert 2010) are $t/t' = 90 \text{ Myrs}$ (or about one-third of an orbital time), $S/S' = 160 \text{ M}_{\odot} \text{ yr}^{-1}$, $M_{\text{gas}}/M'_{\text{gas}} = 1.4 \times 10^{10} \text{ M}_{\odot}$ and $\sigma/\sigma' = 70 \text{ km s}^{-1}$. The scaled Toomre parameter, Q' is related to the actual Toomre parameters by a factor of $\approx 1/2$ to 1, depending on the efficiency at which accretion energy and the mechanical output from stars is converted into turbulence.

The results of this model are shown in Fig. 15. When the coupling efficiency of the mechanical energy from the young stellar population is high, around 5-15%, $Q \sim 1$ through most of the evolution and because of this, the star-formation rate is roughly constant. The energy injection into the ISM from the accretion and star formation is high and therefore, dispersions are also high throughout much of the evolution. With the adopted scalings, the dispersions are about $50\text{-}150 \text{ km s}^{-1}$, and star-formation rates are about $50\text{-}200 \text{ M}_{\odot} \text{ yr}^{-1}$. All of these values are within the range observed in our sample. Star formation increases the Toomre parameter to $Q \sim 1$ throughout the evolution and stabilizes disk star formation. At higher coupling efficiencies, the gas dispersion can be even higher but the star formation is suppressed. Elmegreen & Burkert (2010) set $Q=1$ when Q in their model dropped below one. However, since we allow the energy injection from star formation to evolve with star formation, we find a different time evolution. Unlike in the model of Elmegreen & Burkert (2010), the star-formation rate does not reach the accretion rate until well after the accretion has stopped and the gas fraction has dropped below 50% of the total (gas plus stellar) mass.

When the coupling with the mechanical energy output of the stellar population is weak, the disk is no longer stabilized near $Q \sim 1$ and Q becomes very small (similar to the results of Elmegreen & Burkert 2010). Consequently, star formation increases rapidly and exceeds the accretion rate. This high star-formation rate occurs again when the gas fraction drops below about 50%. In this model, star-formation rates are $\sim 200 \text{ M}_{\odot} \text{ yr}^{-1}$. This is high but reasonable compared to the star-formation rates in our galaxies. The values in Table 1 are generally lower than this, but they have not been corrected for extinction, which is likely to increase them by factors of a few (Lehnert et al. 2009). We note that during the early, gas-rich phase of evolution in these models, the Jeans mass is relatively high which implies that the disks would be very clumpy, especially if the mechanical energy from stars couples very efficiently to the gas (because such galaxies stay relatively gas rich; Elmegreen & Scalo 2004; Elmegreen et al. 2009a,b; Bournaud et al. 2007; Bournaud & Elmegreen 2009; Ceverino et al. 2010).

The basic point illustrated by this simple model is that star formation can play a key role in regulating large-scale instabilities within the disks of distant galaxies. Previous studies have come to the same conclusion in a somewhat different context (e.g., Silk 1997, 2001, 2003; Silk & Norman 2009). What we have added to the analysis is the use of the star formation to drive the line widths (which are a combination of turbulent and bulk motions). In addition, given a sufficiently high coupling efficiency, young stars can control the subsequent star formation in distant galaxies. There does not need to be correspondence between the instantaneous cosmological gas accretion rate and the star-formation rate. In fact, quite the opposite. Smooth constant accretion is probably unrealistic (e.g. Danovich et al. 2012) and what we have shown here is that star formation, even if initiated by the accretion event, does not have to be related closely in time with accretion. The amount of energy available from the

supernovae and stellar winds is much larger in comparison and very early in the evolution begins to control the star-formation history.

5.5. Is the coupling unrealistically efficient?

There are of course the important questions of whether or not coupling efficiencies as high as those that are needed to explain the large line widths are realistic and if the energy output from the young stellar population through SNe and stellar winds can drive the necessary turbulence. Some modeling studies suggest this is not the case (Dekel et al. 2009b; Krumholz & Dekel 2010), while other suggest that it may be (Joung et al. 2009).

Observationally, there are few constraints on what the value of the coupling factor might be. Krumholz & Dekel (2010) criticized the analysis of Lehnert et al. (2009), arguing that the required coupling efficiency between the mechanical energy from star-formation and the ambient ISM is too high. Our analysis in the previous section suggested that coupling efficiencies of 5-15% are necessary to explain the approximate characteristics of distant galaxies, especially the relatively high velocity dispersions. But even these estimates are very uncertain in that we do not really know the dissipation time scales and that changes in the dissipation rate will modify the coupling factor. They must be short, approximately one turnover time scale of turbulence (a few to tens of Myrs), as argued in Lehnert et al. (2009) and as suggested by the model discussed in the previous section and the simulations and physical arguments presented in (e.g. Mac Low 1999; Elmegreen & Scalo 2004; Joung et al. 2009). The model suggests that the dissipation time scale decreases with time and increases with coupling efficiency. Since the dissipation rate is proportional to the ratio of the velocity dispersion and the scale height of the disk, the disk must be thick throughout much of its evolution. This agrees with our finding that the gas has a relatively low ionization (and weak radiation pressure) so it must be widely distributed in the ISM.

While we call this the “coupling factor”, there are various factors that contribute to this coupling. To unwind these, we will use the well studied nucleus of M82 as the analog for our distant galaxies, given that the star formation intensity of M82 on a several 100 pc scale is similar to that of the galaxies presented here. First, the mass ejection from the stellar population must be efficiently thermalized. In a study of the nuclear X-ray emission properties, which probes gas up to temperatures of about $10^{7.8}$ K and directly probes the “piston” driving outflows, Strickland & Heckman (2009) find that on scales of kpc, the thermalization efficiency is 0.3-1.0. The entrainment factor – the amount of ambient ISM that is swept-up, accelerated, and mixed into the hot high pressure plasma – is also important. Again, the modeling of Strickland & Heckman (2009) suggests relatively low entrainment rates of 1-4 times the mass loss of the stellar population in the region surrounding the nucleus of M82. In addition, in the optical emission line gas of M82, large line widths and high pressures are observed (Westmoquette et al. 2009). This suggests that a fraction of the energy from the intense star formation is dissipated in the WIM.

There are several ways in which the coupling between the thermalized mechanical energy from young stars may be enhanced. Star formation which is distributed increases the coupling factor between the mechanical energy and the cold/warm ambient medium (Fragile et al. 2004; Cooper et al. 2009). This enhancement results from the fact that with distributed regions of star formation, say in a clumpy disk, overlapping bubbles of hot plasma begin to interact and cause the formation of dense rims

of gas in this interaction zone (Tenorio-Tagle et al. 2003, 2006). This also has the effect of reducing the opening angles through which the hot plasma can flow (Tenorio-Tagle et al. 2003) which would thereby increase the central pressures in the star forming regions, further enhancing its influence on the surrounding ISM. Our photoionization and simple dynamical modeling implies that our galaxies have a geometrically “thick” (~ 1 kpc) warm ionized medium of moderate densities and low ionization parameters. Such a thick medium would enhance the interaction between the mechanical luminosity of the young stars and the ambient ISM. The strong interaction zones, the reduced opening angle of the outflows, and a thick warm ionized medium would have the effect of smothering the outflow and increasing the efficiency at which the mechanical energy couples to the ambient ISM, and also likely increases the cooling of the hot plasma generated by the collective action of SNe and stellar winds in each star forming clump or region (Wünsch et al. 2008; Hopkins et al. 2012). There is evidence that the optical emission line gas in distant galaxies may be geometrically thick (Epinat et al. 2012, e.g.). In addition, these interacting and overlapping regions of strong mechanical energy input may also drive gas to collapse and form molecular clouds which may be sites of subsequent star formation (Tenorio-Tagle et al. 2005; Hennebelle et al. 2008), thus aiding in completing one part of the gas cycle we are advocating.

Furthermore, we have up to now only considered the influence of the mechanical energy output of the massive stars but not their radiation field (except in the WIM itself). Depending on the star formation history and duration, a significant fraction of up to many times the momentum imparted by the mechanical output of a starburst could be imparted on dusty gas by radiation pressure (Leitherer et al. 1999; Murray et al. 2005). Moreover, if the optical depth to IR photons is high, the radiation pressure may dominate the total momentum output (Hopkins et al. 2011). However, it remains difficult to judge the importance of radiation pressure in the overall pressure (cf. Murray et al. 2005; Silk & Nusser 2010; Ostriker & Shetty 2011; Hopkins et al. 2011). For our discussion, the important point is that radiation pressure is more likely to be effective in imparting momentum to the dense, dusty molecular gas whereas the mechanical energy output will tend to flow around, engulf, and destroy the molecular clouds. Thus radiation pressure may be very effective in driving the large scale kinematics of the denser gas and thus regulate star formation globally.

The coupling efficiency needed to drive the turbulence is dependent on the energy dissipation timescale of the gas. In the range of coupling efficiencies that lead to reasonable results compared to observations, the energy dissipation timescale is in the range of a few to tens of Myrs or in other words, shorter than a dynamical time or the duration of the intense star formation, and approximately as long as one turnover timescale of turbulence for a 1 kpc thick $H\alpha$ emitting layer (see Lehnert et al. 2009). Thus in such a model, the cycle proposed is predicted to be long-lived through repeated cycles of a turbulent cascade driven by the energy input of massive stars. Since the rotational lines of H_2 are one of the dominant coolants of warm molecular gas, and trace the dissipation of supersonic turbulence (e.g. Guillard et al. 2010), observations of distant galaxies with MIRI on the JWST in the infrared will be crucial in constraining the coupling efficiency and testing the scenario we have proposed.

5.6. Summary

Through our analysis of near-infrared integral field spectroscopic observations we found that the optical emission line gas has a high thermal pressure compared to nearby galaxies, and ionization parameters that range from those of giant HII regions to those of diffuse low density gas away from star formation regions, similar to what is observed in nearby normal and starburst galaxies (e.g. Lehnert & Heckman 1996; Wang et al. 1998; Le Tiran et al. 2011b; Kewley & Dopita 2002; Pellegrini et al. 2011). The broad optical emission lines observed ($\sigma_{\text{H}\alpha} \lesssim 50\text{-}250 \text{ km s}^{-1}$) are not mainly due to beam smearing but show that lines are intrinsically broader in regions of more intense star formation. This suggests that the warm ionized gas has a high level of turbulence and bulk motions, and participates in outflows (Le Tiran et al. 2011b; Genzel et al. 2011) that are largely driven by the intense star formation. The high level of turbulence and the influence of intense star formation is consistent with the clumpy nature of distant galaxies (e.g. Elmegreen & Scalo 2004; Elmegreen et al. 2009a,b).

The total pressure of the warm ionized medium appears to be dominated by the thermal pressure as its average volume-weighted density is very low. The relatively low ionization parameters of the emission line gas suggest the thermal pressure in the WIM is due to the mechanical energy output of massive stars and not radiation pressure of the ionizing field.

The evidence we have presented favors the high turbulence being driven by mechanical output of young stars, which is the energy source that regulates the gas to be near the line of disk instability ($Q \sim 1$). The mechanical energy from the intense star-formation is likely efficiently thermalized (Strickland & Heckman 2009), creating large regions of high turbulence. The intense radiation field from young stars may also impart momentum to the gas, depending on the gas column densities and opacity to IR photons. The importance of the radiation pressure is that it may couple to the dense dusty gas more effectively than the mechanical energy output, and thus regulate star formation globally.

Both the mechanical energy (through the thermalized hot plasma generated by stellar winds and supernovae) and the radiation field of young stars generate turbulence, bulk motions and high turbulent pressures in the gas which are similar to the thermal pressure of the WIM and the hydrostatic pressure. However, for the turbulent pressure to be similar to the hydrostatic pressure, the high velocity dispersions observed in the WIM have to be (at least partially) transferred to the dense molecular gas, which likely has a much larger mass and average volume weighted density than the recombining gas. Such transfer may happen because at high pressures the recombining gas is unstable and will quickly cool and collapse to a cold neutral phase (Wolfire et al. 1995), and become molecular if dusty (Guillard et al. 2009). Since this collapse and cooling time scale is much shorter than the dynamical time scale, the kinematics of the WIM and the CNM should be similar (Guillard et al. 2012). This leads to the formation of gravitationally bound clouds which have dissipated their gravitational energy as turbulence in the molecular gas. Some of these clouds will form stars, and some may be destroyed by the intense energy output of massive stars. The ISM will quickly reach a dynamical equilibrium, due to the relatively short timescales for gas cooling, and the formation of molecular gas and gravitationally bound clouds. The short timescale compared to those of star formation indicates there is sufficient time for repeated cycles, allowing for the build-up of the stellar population in our distant galaxies.

To explain the observed star formation intensity – line width distribution, we made a simple model for the energy flow in a galaxy undergoing both intense gas accretion and star formation. This model suggests that only a few to perhaps 15% of the injected energy from stars is required to drive the high level of turbulence we observe. This relatively small fraction of the total energy injection is reasonable.

If the high dispersion observed in the optical emission line gas is due to turbulence and if the denser phases of the ISM share such high turbulence, then the gas and stellar mass surface densities in $z \sim 2$ galaxies are consistent with $Q \sim 1$ and star formation is a plausible hypothesis for driving the gas towards the line of stability. If so, this would be an avenue for self-regulated star formation in distant galaxies. More observations, especially of the warm molecular gas in distant intensely star forming galaxies are needed to gauge whether or not this picture is correct.

Acknowledgements. The work of LLT, MDL and PDM is supported by a grant from the Agence Nationale de la Recherche (ANR) in France. MDL and NPHN wish to thank the CNRS for their continuing support.

References

- Agertz, O., Lake, G., Teyssier, R., et al. 2009, MNRAS, 392, 294
 Aravena, M., Carilli, C., Daddi, E., et al. 2010, ApJ, 718, 177
 Barden, M., Rix, H.-W., Somerville, R. S., et al. 2005, ApJ, 635, 959
 Basu-Zych, A. R., Gonçalves, T. S., Overzier, R., et al. 2009, ApJ, 699, L118
 Blitz, L. & Rosolowsky, E. 2006, ApJ, 650, 933
 Bournaud, F. & Elmegreen, B. G. 2009, ApJ, 694, L158
 Bournaud, F., Elmegreen, B. G., & Elmegreen, D. M. 2007, ApJ, 670, 237
 Brooks, A. M., Governato, F., Quinn, T., Brook, C. B., & Wadsley, J. 2009, ApJ, 694, 396
 Burkert, A., Genzel, R., Bouché, N., et al. 2010, ApJ, 725, 2324
 Cacciato, M., Dekel, A., & Genel, S. 2012, MNRAS, 421, 818
 Ceverino, D., Dekel, A., & Bournaud, F. 2010, MNRAS, 404, 2151
 Chevalier, R. A. & Clegg, A. W. 1985, Nature, 317, 44
 Chilingarian, I. V., Di Matteo, P., Combes, F., Melchior, A., & Semelin, B. 2010, A&A, 518, A61+
 Combes, F., García-Burillo, S., Braine, J., et al. 2011, A&A
 Conselice, C. J., Rajgor, S., & Myers, R. 2008, MNRAS, 386, 909
 Cooper, J. L., Bicknell, G. V., Sutherland, R. S., & Bland-Hawthorn, J. 2009, ApJ, 703, 330
 Cox, D. P. 2005, ARA&A, 43, 337
 Croton, D. J., Springel, V., White, S. D. M., et al. 2006, MNRAS, 365, 11
 Daddi, E., Bournaud, F., Walter, F., et al. 2010, ApJ, 713, 686
 Daddi, E., Dickinson, M., Morrison, G., et al. 2007, ApJ, 670, 156
 Dannerbauer, H., Daddi, E., Riechers, D. A., et al. 2009, ApJ, 698, L178
 Danovich, M., Dekel, A., Hahn, O., & Teyssier, R. 2012, MNRAS, 422, 1732
 de Ravel, L., Le Fèvre, O., Tresse, L., et al. 2009, A&A, 498, 379
 Dekel, A., Birnboim, Y., Engel, G., et al. 2009a, Nature, 457, 451
 Dekel, A., Sari, R., & Ceverino, D. 2009b, ApJ, 703, 785
 Di Matteo, P., Bournaud, F., Martig, M., et al. 2008, A&A, 492, 31
 Di Matteo, P., Jog, C. J., Lehnert, M. D., Combes, F., & Semelin, B. 2009, A&A, 501, L9
 Dib, S., Bell, E., & Burkert, A. 2006, ApJ, 638, 797
 Elbaz, D., Daddi, E., Le Borgne, D., et al. 2007, A&A, 468, 33
 Elbaz, D., Dickinson, M., Hwang, H. S., et al. 2011, ArXiv e-prints
 Elmegreen, B. G. & Burkert, A. 2010, ApJ, 712, 294
 Elmegreen, B. G., Elmegreen, D. M., Fernandez, M. X., & Lemonias, J. J. 2009a, ApJ
 Elmegreen, B. G. & Scalo, J. 2004, ARA&A, 42, 211
 Elmegreen, D. M., Elmegreen, B. G., Marcus, M. T., et al. 2009b, ApJ, 701, 306
 Epinat, B., Amram, P., Balkowski, C., & Marcelin, M. 2010, MNRAS, 401, 2113
 Epinat, B., Contini, T., Le Fèvre, O., et al. 2009, A&A, 504, 789
 Epinat, B., Tasca, L., Amram, P., et al. 2012, A&A, 539, A92
 Erb, D. K., Steidel, C. C., Shapley, A. E., et al. 2006, ApJ, 647, 128
 Erroz-Ferrer, S., Knäpen, J. H., Font, J., et al. 2012, MNRAS, 427, 2938
 Fathi, K., Beckman, J. E., Zurita, A., et al. 2007, A&A, 466, 905
 Ferland, G. J., Korista, K. T., Verner, D. A., et al. 1998, PASP, 110, 761
 Ferrara, A. 1993, ApJ, 407, 157
 Förster Schreiber, N. M., Genzel, R., Bouché, N., et al. 2009, ApJ, 706, 1364
 Förster Schreiber, N. M., Lehnert, M. D., Bouché, N., et al. 2006, ApJ, 645, 1062
 Förster Schreiber, N. M., Shapley, A. E., Erb, D. K., et al. 2011, ApJ, 731, 65
 Fragile, P. C., Murray, S. D., & Lin, D. N. C. 2004, ApJ, 617, 1077

- Genzel, R., Newman, S., Jones, T., et al. 2011, *ApJ*, 733, 101
- Gonçalves, T. S., Basu-Zych, A., Overzier, R., et al. 2010, *ApJ*, 724, 1373
- Green, A. W., Glazebrook, K., McGregor, P. J., et al. 2010, *Nature*, 467, 684
- Guillard, P., Boulanger, F., Cluver, M. E., et al. 2010, *A&A*, 518, A59
- Guillard, P., Boulanger, F., Pineau Des Forêts, G., & Appleton, P. N. 2009, *A&A*, 502, 515
- Guillard, P., Boulanger, F., Pineau des Forêts, G., et al. 2012, *ApJ*, 749, 158
- Heckman, T. M., Armus, L., & Miley, G. K. 1990, *ApJS*, 74, 833
- Hennelle, P., Banerjee, R., Vázquez-Semadeni, E., Klessen, R. S., & Audit, E. 2008, *A&A*, 486, L43
- Hopkins, P. F., Quataert, E., & Murray, N. 2011, *MNRAS*, 417, 950
- Hopkins, P. F., Quataert, E., & Murray, N. 2012, *MNRAS*, 2655
- Jog, C. J. 1996, *MNRAS*, 278, 209
- Joung, M. R., Mac Low, M., & Bryan, G. L. 2009, *ApJ*, 704, 137
- Kennicutt, Jr., R. C. 1998, *ApJ*, 498, 541
- Kereš, D., Katz, N., Fardal, M., Davé, R., & Weinberg, D. H. 2009, *MNRAS*, 395, 160
- Kewley, L. J. & Dopita, M. A. 2002, *ApJS*, 142, 35
- Krumholz, M. R. & Dekel, A. 2010, *MNRAS*, 406, 112
- Krumholz, M. R. & Matzner, C. D. 2009, *ApJ*, 703, 1352
- Law, D. R., Steidel, C. C., Erb, D. K., et al. 2007, *ApJ*, 669, 929
- Law, D. R., Steidel, C. C., Erb, D. K., et al. 2009, *ApJ*, 697, 2057
- Le Tiran, L., Lehnert, M. D., Di Matteo, P., Nesvadba, N. P. H., & van Driel, W. 2011a, *A&A*, 530, L6
- Le Tiran, L., Lehnert, M. D., van Driel, W., Nesvadba, N. P. H., & Di Matteo, P. 2011b, *A&A*, 534, L4
- Lehnert, M. D. & Heckman, T. M. 1996, *ApJ*, 462, 651
- Lehnert, M. D., Heckman, T. M., & Weaver, K. A. 1999, *ApJ*, 523, 575
- Lehnert, M. D., Nesvadba, N. P. H., Tiran, L. L., et al. 2009, *ApJ*, 699, 1660
- Leitherer, C., Schaerer, D., Goldader, J. D., et al. 1999, *ApJS*, 123, 3
- Leroy, A. K., Walter, F., Brinks, E., et al. 2008, *AJ*, 136, 2782
- López-Hernández, J., Terlevich, E., Terlevich, R., et al. 2013, *MNRAS*, 430, 472
- Mac Low, M.-M. 1999, *ApJ*, 524, 169
- Mac Low, M.-M. & Klessen, R. S. 2004, *Reviews of Modern Physics*, 76, 125
- Madau, P., Ferguson, H. C., Dickinson, M. E., et al. 1996, *MNRAS*, 283, 1388
- Menéndez-Delmestre, K., Blain, A. W., Swinbank, M., et al. 2013, *ApJ*, 767, 151
- Moran, E. C., Lehnert, M. D., & Helfand, D. J. 1999, *ApJ*, 526, 649
- Murray, N., Quataert, E., & Thompson, T. A. 2005, *ApJ*, 618, 569
- Nesvadba, N. P. H., Lehnert, M. D., De Breuck, C., Gilbert, A. M., & van Breugel, W. 2008, *A&A*, 491, 407
- Nesvadba, N. P. H., Lehnert, M. D., Eisenhauer, F., et al. 2006, *ApJ*, 650, 693
- Nesvadba, N. P. H., Lehnert, M. D., Genzel, R., et al. 2007, *ApJ*, 657, 725
- Norman, C. A. & Ferrara, A. 1996, *ApJ*, 467, 280
- Ostriker, E. C. & Shetty, R. 2011, *ApJ*, 731, 41
- Pellegrini, E. W., Baldwin, J. A., & Ferland, G. J. 2011, *ApJ*, 738, 34
- Qu, Y., Di Matteo, P., Lehnert, M. D., & van Driel, W. 2011, *ArXiv e-prints*
- Romeo, A. B. & Wiegert, J. 2011, *MNRAS*, 416, 1191
- Semelin, B. & Combes, F. 2002, *A&A*, 388, 826
- Shapley, A. E., Steidel, C. C., Pettini, M., & Adelberger, K. L. 2003, *ApJ*, 588, 65
- Shen, S., Mo, H. J., White, S. D. M., et al. 2003, *MNRAS*, 343, 978
- Silk, J. 1997, *ApJ*, 481, 703
- Silk, J. 2001, *MNRAS*, 324, 313
- Silk, J. 2003, *MNRAS*, 343, 249
- Silk, J. & Norman, C. 2009, *ApJ*, 700, 262
- Silk, J. & Nusser, A. 2010, *ApJ*, 725, 556
- Steidel, C. C., Erb, D. K., Shapley, A. E., et al. 2010, *ApJ*, 717, 289
- Strickland, D. K. & Heckman, T. M. 2009, *ApJ*, 697, 2030
- Suchkov, A. A., Berman, V. G., Heckman, T. M., & Balsara, D. S. 1996, *ApJ*, 463, 528
- Swinbank, A. M., Smail, I., Sobral, D., et al. 2012, *ApJ*, 760, 130
- Swinbank, M., Papadopoulos, P., Cox, P., et al. 2011, *ArXiv e-prints*
- Tacconi, L. J., Genzel, R., Neri, R., et al. 2010, *Nature*, 463, 781
- Tamburro, D., Rix, H.-W., Leroy, A. K., et al. 2009, *AJ*, 137, 4424
- Taylor, E. N., Franx, M., Glazebrook, K., et al. 2010, *ApJ*, 720, 723
- Tenorio-Tagle, G., Muñoz-Tuñón, C., Pérez, E., Silich, S., & Telles, E. 2006, *ApJ*, 643, 186
- Tenorio-Tagle, G., Silich, S., & Muñoz-Tuñón, C. 2003, *ApJ*, 597, 279
- Tenorio-Tagle, G., Silich, S., Rodríguez-González, A., & Muñoz-Tuñón, C. 2005, *ApJ*, 628, L13
- Terlevich, R. & Melnick, J. 1981, *MNRAS*, 195, 839
- Vergani, D., Epinat, B., Contini, T., et al. 2012, *A&A*, 546, A118
- Wada, K., Meurer, G., & Norman, C. A. 2002, *ApJ*, 577, 197
- Wang, B. & Silk, J. 1994, *ApJ*, 427, 759
- Wang, J., Heckman, T. M., & Lehnert, M. D. 1998, *ApJ*, 509, 93
- Westmoquette, M. S., Gallagher, J. S., Smith, L. J., et al. 2009, *ApJ*, 706, 1571
- Westmoquette, M. S., Smith, L. J., Gallagher, III, J. S., et al. 2007, *ApJ*, 671, 358
- Wilson, C. D., Warren, B. E., Irwin, J., et al. 2011, *MNRAS*, 410, 1409
- Wisnioski, E., Glazebrook, K., Blake, C., et al. 2012, *MNRAS*, 422, 3339
- Wolfire, M. G., Hollenbach, D., McKee, C. F., Tielens, A. G. G. M., & Bakes, E. L. O. 1995, *ApJ*, 443, 152
- Wünsch, R., Tenorio-Tagle, G., Palouš, J., & Silich, S. 2008, *ApJ*, 683, 683
- Yuma, S., Ohta, K., Yabe, K., Kajisawa, M., & Ichikawa, T. 2011, *ApJ*, 736, 92

Table 1. Properties of the High- z Galaxies

Object (1)	Int (2)	Line (3)	z (4)	σ (5)	Flux (6)	SFR (7)	SB limit (8)	r_{iso} (9)
BzK-15504 ^b	20400	H α	2.3816 \pm 0.0014	110 \pm 5	5.96 \pm 0.27	209 \pm 10	2.1	5.8
		[NII] λ 6583	2.3818 \pm 0.0016	134 \pm 12	2.44 \pm 0.20			
BzK-15504	20400	H α	2.3822 \pm 0.0020	164 \pm 7	7.10 \pm 0.27	249 \pm 10	5.8	9.3
		[NII] λ 6583	2.3819 \pm 0.0016	133 \pm 14	1.96 \pm 0.21			
BzK-6004	36000	H α	2.3865 \pm 0.0013	105 \pm 5	4.31 \pm 0.19	152 \pm 7	4.2	8.7
		[NII] λ 6583	2.3866 \pm 0.0010	67 \pm 6	1.77 \pm 0.15			
BzK-6397	9600	H α	1.5133 \pm 0.0012	121 \pm 6	2.79 \pm 0.12	32 \pm 2	2.3	10.5
		[NII] λ 6583	1.5136 \pm 0.0016	178 \pm 17	1.14 \pm 0.10			
CDFS-GK1084	7200	H α	1.5521 \pm 0.0009	87 \pm 8	0.38 \pm 0.03	4 \pm 1	2.9	4.4
		[NII] λ 6583	1.5527 \pm 0.0009	88 \pm 20	0.14 \pm 0.03			
CDFS-GK2252	18000	H α	2.4080 \pm 0.0014	111 \pm 9	0.90 \pm 0.06	32 \pm 3	7.8	4.7
		[NII] λ 6583	2.4073 \pm 0.0013	101 \pm 28	0.21 \pm 0.06			
CDFS-GK2363	17400	H α	2.4512 \pm 0.0014	105 \pm 8	1.13 \pm 0.09	42 \pm 4	8.1	4.4
		[NII] λ 6583	2.4508 \pm 0.0009	60 \pm 15	0.25 \pm 0.06			
CDFS-GK2471	16800	H α	2.4319 \pm 0.0019	159 \pm 8	2.20 \pm 0.11	81 \pm 5	8.3	5.3
		[NII] λ 6583	2.4350 \pm 0.0005	...	<0.34 ^c			
DEEP2-32002481	6600	H α	1.3880 \pm 0.0014	156 \pm 19	2.77 \pm 0.32	25 \pm 3	2.5	9.8
		[NII] λ 6583	1.3897 \pm 0.0017	209 \pm 65	1.20 \pm 0.37			
DEEP2-32007614	5400	H α	1.3716 \pm 0.0010	110 \pm 8	1.12 \pm 0.08	10 \pm 1	6.9	3.9
		[NII] λ 6583	1.3718 \pm 0.0006	42 \pm 6	0.46 \pm 0.06			
DEEP2-32100778	6000	H α	1.3918 \pm 0.0006	41 \pm 4	3.54 \pm 0.27	33 \pm 3	3.9	8.8
		[NII] λ 6583	1.3919 \pm 0.0007	59 \pm 14	1.36 \pm 0.31			
DEEP2-32013051	5400	H α	1.3950 \pm 0.0011	118 \pm 9	2.45 \pm 0.18	23 \pm 2	2.8	7.7
		[NII] λ 6583	1.3951 \pm 0.0011	124 \pm 16	1.57 \pm 0.19			
DEEP2-32015443	6600	H α	1.3822 \pm 0.0009	85 \pm 13	1.48 \pm 0.22	13 \pm 3	6.0	6.7
		[NII] λ 6583	1.3824 \pm 0.0009	83 \pm 28	0.54 \pm 0.18			
DEEP2-32015501	10800	H α	1.3919 \pm 0.0007	58 \pm 5	2.47 \pm 0.18	23 \pm 2	3.8	9.5
		[NII] λ 6583	1.3921 \pm 0.0006	32 \pm 12	0.38 \pm 0.14			
DEEP2-32021317	5400	H α	1.3815 \pm 0.0017	198 \pm 20	2.92 \pm 0.28	26 \pm 3	4.3	8.3
		[NII] λ 6583	1.3822 \pm 0.0028	348 \pm 39	3.34 \pm 0.37			
DEEP2-32021394	5400	H α	1.3735 \pm 0.0009	92 \pm 9	2.78 \pm 0.25	25 \pm 3	4.0	9.5
		[NII] λ 6583	1.3753 \pm 0.0013	156 \pm 34	1.29 \pm 0.28			
DEEP2-32029850	6600	H α	1.3952 \pm 0.0009	81 \pm 22	0.13 \pm 0.03	1 \pm 1	3.6	2.5
		[NII] λ 6583	1.3960 \pm 0.0010	108 \pm 36	0.09 \pm 0.03			
DEEP2-32037003	5400	H α	1.3985 \pm 0.0014	157 \pm 7	5.50 \pm 0.24	52 \pm 3	3.6	9.6
		[NII] λ 6583	1.3987 \pm 0.0010	103 \pm 15	1.40 \pm 0.19			
ECDFS-10525	5400	H α	2.0261 \pm 0.0029	278 \pm 27	6.90 \pm 0.67	163 \pm 16	11.5	7.8
		[NII] λ 6583	2.0271 \pm 0.0014	118 \pm 20	2.59 \pm 0.43			
ECDFS-2896	3600	H α	2.3060 \pm 0.0017	137 \pm 17	1.55 \pm 0.19	50 \pm 7	16.0	3.5
		[NII] λ 6583	2.3050 \pm 0.0019	155 \pm 29	1.14 \pm 0.21			
F257	21600	H α	2.0264 \pm 0.0014	122 \pm 11	1.92 \pm 0.16	45 \pm 4	2.8	9.3
		[NII] λ 6583	2.0255 \pm 0.0011	89 \pm 29	0.38 \pm 0.12			
K20-ID4	9900	H α	1.5934 \pm 0.0008	62 \pm 4	2.85 \pm 0.14	37 \pm 2	1.7	8.3
		[NII] λ 6583	1.5937 \pm 0.0008	64 \pm 7	0.79 \pm 0.08			
K20-ID5	12000	H α	2.2240 \pm 0.0022	195 \pm 10	2.97 \pm 0.14	88 \pm 5	5.6	6.1
		[NII] λ 6583	2.2240 \pm 0.0029	260 \pm 23	1.83 \pm 0.16			
K20-ID7	25200	H α	2.2233 \pm 0.0017	148 \pm 7	4.38 \pm 0.18	130 \pm 6	2.9	9.4
		[NII] λ 6583	2.2243 \pm 0.0013	111 \pm 14	0.87 \pm 0.11			
K20-ID8	15000	H α	2.2230 \pm 0.0011	89 \pm 5	2.20 \pm 0.11	65 \pm 4	3.7	7.5
		[NII] λ 6583	2.2241 \pm 0.0015	123 \pm 17	0.74 \pm 0.10			
Q1623-BX376	17400	H α	2.4080 \pm 0.0011	83 \pm 6	0.36 \pm 0.02	12 \pm 1	4.6	3.5
		[NII] λ 6583	2.4085 \pm 0.0007	32 \pm 11	0.05 \pm 0.02			
Q1623-BX447	13800	H α	2.1471 \pm 0.0014	118 \pm 11	1.07 \pm 0.10	29 \pm 3	4.2	5.8
		[NII] λ 6583	2.1498 \pm 0.0005	...	<0.35 ^c			
Q1623-BX455	12000	H α	2.4065 \pm 0.0014	107 \pm 8	1.41 \pm 0.09	50 \pm 4	10.7	4.2
		[NII] λ 6583	2.4080 \pm 0.0015	124 \pm 34	0.35 \pm 0.09			
Q1623-BX543	8400	H α	2.5204 \pm 0.0017	137 \pm 6	5.94 \pm 0.26	239 \pm 11	12.5	6.1
		[NII] λ 6583	2.5160 \pm 0.0011	72 \pm 21	0.68 \pm 0.19			
Q1623-BX599	5400	H α	2.3305 \pm 0.0019	160 \pm 7	5.99 \pm 0.24	199 \pm 9	8.2	6.2
		[NII] λ 6583	2.3302 \pm 0.0011	85 \pm 17	0.76 \pm 0.15			
Q1623-BX663	33300	H α	2.4253 \pm 0.0026	219 \pm 12	1.96 \pm 0.11	72 \pm 5	4.3	6.2
		[NII] λ 6583	2.4265 \pm 0.0038	325 \pm 58	0.75 \pm 0.13			

Table 1. continued.

Object (1)	Int (2)	Line (3)	z (4)	σ (5)	Flux (6)	SFR (7)	SB limit (8)	r_{iso} (9)
Q2343-BX389	14400	H α	2.1716 \pm 0.0020	180 \pm 7	4.59 \pm 0.17	128 \pm 5	3.4	8.5
		[NII] λ 6583	2.1727 \pm 0.0014	122 \pm 27	0.69 \pm 0.15			
Q2343-BX502	9600	H α	2.1550 \pm 0.0008	52 \pm 3	1.82 \pm 0.09	50 \pm 3	2.8	7.7
		[NII] λ 6583	2.1571 \pm 0.0010	...	0.23 ^d			
Q2343-BX528	34200	H α	2.2684 \pm 0.0015	128 \pm 6	2.26 \pm 0.10	70 \pm 4	4.2	7.5
		[NII] λ 6583	2.2691 \pm 0.0010	72 \pm 10	0.41 \pm 0.05			
Q2343-BX610	21600	H α	2.2098 \pm 0.0018	163 \pm 7	7.91 \pm 0.32	231 \pm 10	3.7	9.3
		[NII] λ 6583	2.2105 \pm 0.0013	106 \pm 6	2.49 \pm 0.13			
Q2346-BX482	31200	H α	2.2562 \pm 0.0015	131 \pm 6	4.09 \pm 0.17	126 \pm 6	3.4	9.0
		[NII] λ 6583	2.2566 \pm 0.0010	70 \pm 10	0.48 \pm 0.06			
SA12-5241	7200	H α	1.3617 \pm 0.0007	53 \pm 3	1.46 \pm 0.07	13 \pm 1	4.3	6.0
		[NII] λ 6583	1.3619 \pm 0.0006	37 \pm 4	0.62 \pm 0.06			
SA12-6192	10800	H α	1.5038 \pm 0.0008	62 \pm 5	0.69 \pm 0.05	7 \pm 1	1.8	5.7
		[NII] λ 6583	1.5038 \pm 0.0009	84 \pm 12	0.40 \pm 0.06			
SA12-6339	19200	H α	2.2963 \pm 0.0013	102 \pm 5	3.33 \pm 0.15	107 \pm 5	4.3	6.0
		[NII] λ 6583	2.2950 \pm 0.0016	129 \pm 26	0.61 \pm 0.12			
SA12-8768	10800	H α	2.1875 \pm 0.0010	73 \pm 4	2.31 \pm 0.12	66 \pm 4	5.5	6.6
		[NII] λ 6583	2.1875 \pm 0.0011	85 \pm 21	0.44 \pm 0.10			
SA15-5365	9000	H α	1.5340 \pm 0.0011	117 \pm 12	1.10 \pm 0.10	13 \pm 2	2.1	6.8
		[NII] λ 6583	1.5323 \pm 0.0010	100 \pm 40	0.19 \pm 0.07			
SINS-4751	3600	H α	2.2651 \pm 0.0011	78 \pm 4	3.12 \pm 0.16	97 \pm 5	6.2	5.8
		[NII] λ 6583	2.2651 \pm 0.0010	69 \pm 17	0.48 \pm 0.11			
SSA-22a-MD041	21600	H α	2.1632 \pm 0.0014	122 \pm 6	3.54 \pm 0.16	98 \pm 5	2.9	8.3
		[NII] λ 6583	2.1627 \pm 0.0016	142 \pm 39	0.50 \pm 0.13			
VVDS-020147106	7200	H α	1.5182 \pm 0.0008	76 \pm 4	5.37 \pm 0.27	62 \pm 4	4.1	7.6
		[NII] λ 6583	1.5183 \pm 0.0007	40 \pm 13	0.31 \pm 0.10			
VVDS-020261328	3600	H α	1.5276 \pm 0.0008	71 \pm 4	1.00 \pm 0.06	11 \pm 1	7.9	4.3
		[NII] λ 6583	1.5279 \pm 0.0006	39 \pm 13	0.12 \pm 0.04			
VVDS-220014252	7200	H α	1.3090 \pm 0.0011	130 \pm 6	7.84 \pm 0.35	63 \pm 3	5.6	8.5
		[NII] λ 6583	1.3090 \pm 0.0011	128 \pm 35	1.02 \pm 0.28			
VVDS-220015726	10800	H α	1.2920 \pm 0.0012	140 \pm 7	6.63 \pm 0.30	51 \pm 3	5.2	7.7
		[NII] λ 6583	1.2919 \pm 0.0010	111 \pm 17	1.09 \pm 0.16			
VVDS-220544103	7200	H α	1.3955 \pm 0.0010	103 \pm 5	7.77 \pm 0.35	73 \pm 4	5.6	8.7
		[NII] λ 6583	1.3960 \pm 0.0012	141 \pm 23	1.55 \pm 0.25			
VVDS-220584167	7200	H α	1.4643 \pm 0.0012	125 \pm 6	9.37 \pm 0.42	99 \pm 5	2.6	11.5
		[NII] λ 6583	1.4645 \pm 0.0010	98 \pm 10	1.94 \pm 0.18			
VVDS-220596913	10800	H α	1.2649 \pm 0.0010	107 \pm 5	4.11 \pm 0.18	30 \pm 2	3.3	8.5
		[NII] λ 6583	1.2654 \pm 0.0011	125 \pm 31	0.70 \pm 0.17			
ZC-1101592	3600	H α	1.4034 \pm 0.0013	150 \pm 16	1.07 \pm 0.11	10 \pm 2	10.6	4.1
		[NII] λ 6583	1.4035 \pm 0.0006 ^d	7 \pm 2 ^d	0.24 \pm 0.07 ^d			
ZC-782941 ^b	13800	H α	2.1813 \pm 0.0016	144 \pm 6	3.14 \pm 0.13	89 \pm 4	3.1	4.1
		[NII] λ 6583	2.1814 \pm 0.0010	77 \pm 10	0.74 \pm 0.09			
ZC-782941 ^a	7200	H α	2.1811 \pm 0.0015	133 \pm 6	4.97 \pm 0.21	140 \pm 6	6.2	7.2
		[NII] λ 6583	2.1812 \pm 0.0010	76 \pm 19	0.71 \pm 0.17			

Table 1. Column (1) – Object designation. ^a denotes a 250 mas pixel scale plus adoptive optics, and ^b a 100 mas pixel scale plus adaptive optics. No indication denotes that the data were taken without the benefit of AO, and at 250 mas pixel⁻¹; Column (2) – Integration time in seconds; Column (3) – Line identifications; Column (4) – Redshifts of the H α and [NII] λ 6583 lines in the integrated spectrum. By integrated spectrum, we mean the sum of the fluxes from each pixel with an H α line signal-to-noise ratio $\gtrsim 3$ in a specific data cube (see column 8 for the 3σ surface brightness detection limits). For each object, the sum for the [NII] λ 6583 emission line was determined over the same aperture as for H α ; Column (5) – H α line velocity dispersion of the integrated spectrum of each galaxy, corrected for instrumental resolution and in units of km s⁻¹; Column (6) – H α and [NII] λ 6583 line fluxes of the integrated spectrum in units of 10⁻¹⁶ erg s⁻¹ cm⁻². ^cThe [NII] line is not detected and the value given is the 3- σ upper limit, for a line width equal to that of the H α line, and ^dThe estimated line characteristics are influenced significantly by a nearby night sky line; Column (7) – Star Formation Rate, in M $_{\odot}$ yr⁻¹, estimated from the total H α luminosity following (Kennicutt 1998). These values have not been corrected for extinction, which is likely to increase them by a factor of a few (see text); Column (8) – H α surface brightness detection limit in units of 10⁻¹⁹ erg s⁻¹ cm⁻², at a signal-to-noise level of S/N \approx 3. These are average values over a 3 \times 3 pixel area; Column (9) – Isophotal radius, r_{iso} , defined as $A_{\text{iso}} = \pi r_{\text{iso}}^2$. The isophotal area, A_{iso} , is defined as the projected area on the sky above a signal-to-noise level of 3 in the H α data. r_{iso} is in kpc.